Plasma Chemistry and Plasma Processing
https://doi.org/10.1007/s11090-020-10121-y

ORIGINAL PAPER

Modeling of Atmospheric-Pressure Dielectric Barrier Discharges in Argon with Small Admixtures of Tetramethylsilane

Detlef Loffhagen[1] · Markus M. Becker[1] · Andreas K. Czerny[2,3] · Claus-Peter Klages[2]

Received: 30 June 2020 / Accepted: 19 August 2020

Abstract
A time-dependent, spatially one-dimensional fluid-Poisson model is applied to analyze the impact of small amounts of tetramethylsilane (TMS) as precursor on the discharge characteristics of an atmospheric-pressure dielectric barrier discharge (DBD) in argon. Based on an established reaction kinetics for argon, it includes a plasma chemistry for TMS, which is validated by measurements of the ignition voltage at the frequency $f = 86.2\,\mathrm{kHz}$ for TMS amounts of up to 200 ppm. Details of both a reduced Ar-TMS reaction kinetics scheme and an extended plasma-chemistry model involving about 60 species and 580 reactions related to TMS are given. It is found that good agreement between measured and calculated data can be obtained, when assuming that 25% of the reactions of TMS with excited argon atoms with a rate coefficient of $3.0 \times 10^{-16}\,\mathrm{m^3/s}$ lead to the production of electrons due to Penning ionization. Modeling results for an applied voltage $U_{a,0} = 4\,\mathrm{kV}$ show that TMS is depleted during the residence time of the plasma in the DBD, where the percentage consumption of TMS decreases with increasing TMS fraction because only a finite number of excited argon species is available to dissociate and/or ionize the precursor via energy transfer. Main species resulting from that TMS depletion are presented and discussed. In particular, the analysis clearly indicates that trimethylsilyl cations can be considered to be mainly responsible for the film formation.

Keywords Dielectric barrier discharges · Tetramethylsilane · Numerical modeling · Plasma polymerization

✉ Detlef Loffhagen
loffhagen@inp-greifswald.de

[1] Leibniz Institute for Plasma Science and Technology, Felix-Hausdorff-Str. 2, 17489 Greifswald, Germany

[2] Institute for Surface Technology, Technische Universität Braunschweig, Bienroder Weg 54 E, 38108 Braunschweig, Germany

[3] Present Address: Institute of Applied Materials - Applied Material Physics, Karlsruhe Institute of Technology, Herrmann-von-Helmholtz-Platz 1, 76344 Eggenstein-Leopoldshafen, Germany

Published online: 07 October 2020

Introduction

Tetramethylsilane (TMS, $(CH_3)_4Si$), one of the most simple organosilicon compound (organosilane, alkylsilane), has frequently been used as a precursor for plasma-enhanced chemical vapor deposition (PECVD) of silicon- and carbon-containing thin films [1–11]. The deposition process is also termed "plasma polymerization"—and the deposits "plasma polymer"—if a relatively large "organic" character of the precursor (monomer) is retained in the film, observable, e.g., as a major content of CH_x moeities. Aside from other potential purposes, TMS-derived thin films have been of interest as insulators with low dielectric constants for microelectronic applications ("low-k films") [7–9, 11]. TMS is also a major reaction product in processing plasmas fed with more complex organosilicon monomers such as hexamethyldisiloxane (HMDSO) [12–14]. Owing to its low boiling point of only 300 K [15], TMS is an extremely flammable liquid, its vapor forming explosive mixtures with air. Taking into account the corresponding hazards of working with TMS is of special importance for atmospheric-pressure plasma processes.

Thin film deposition from TMS has usually been performed by means of low-temperature discharge plasmas at low pressure. In addition to the plasma polymerization in pure TMS vapor [2, 6, 7, 11, 16, 17], TMS-vapor mixtures diluted by Ar [3, 4, 10, 18–20], O_2 [7, 9, 11], O_2 and Ar [9], and SiH_4 with N_2O as the oxidant gas [8] were investigated experimentally. Few of these experimental studies were assisted by theoretical and modeling analyzes. By employing the general convective diffusion equation, a simple analytical expression of the deposition rate in Ar-TMS mixtures was obtained in [4]. Furthermore, preliminary modeling of the electrical discharge of a capacitively coupled, low-frequency device in low-pressure Ar-TMS mixtures based on a one-dimensional fluid model was reported in [19, 20].

The deposition of thin functional films using PECVD at atmospheric pressure has gained great scientific and technical interest during the last two decades [21, 22]. In contrast to low-pressure techniques, suffering from high costs of equipment and difficult integration into in-line production processes [23], atmospheric-pressure systems avoid the need for expensive vacuum equipment, allow easier and continuous processing, and make it even possible to treat materials and geometries, which are difficult to handle at reduced pressure conditions.

Atmospheric-pressure plasma polymerization of TMS has recently been performed using different discharge configurations. A radio-frequency glow-discharge system was applied in [24] to generate organic-inorganic hybrid coatings in a plasma generated with a TMS precursor concentration of 0.01−0.04 vol% in He carrier gas. An atmospheric-pressure plasma jet in He with a few vol. % TMS was used in [25–29] to improve the surface hydrophobicity of imitation leather with polyester surface. Furthermore, Haq et al. [30] recently used an atmospheric-pressure microplasma reactor fed by an Ar-TMS mixture containing up to 3500 ppm TMS to study its dissociation for the growth of SiC nanocrystals.

While plasma jets are especially developed for a localized treatment, dielectric barrier discharges (DBDs) are more suitable for the treatment of larger surfaces and they have widely been applied as a source for PECVD processes [31]. A new kind of reactor for plasma treatments based on DBDs, involving a gradient mixer and a homogenizer in the gas-supply line to enable a concentration gradient of the percursor or another relevant gas species oriented perpendicular to the flow direction, was presented in [32] and tested using plasma polymerization of several precursors including mixtures of Ar (or Ar mixed with 2% Xe) and small amounts of up to about 750 ppm of TMS vapor.

The present paper deals with the analysis of atmospheric-pressure DBDs in argon with small amounts of TMS as precursor by means of numerical modeling. It refers to the plane-parallel discharge configuration with lateral gas flow injection described in [33]. The time-dependent, spatially one-dimensional fluid-Poisson model takes into account the spatial variation of the discharge plasma between plane-parallel dielectrics covering the electrodes. It is based on the DBD model for argon reported in [34], which has been extended by collision processes for the precursor gas TMS and resulting reaction procucts. The basic reaction kinetics scheme includes 26 collision processes of TMS as well as further 16 reactions related to collisions of the trimethylsilyl cation ($(CH_3)_3Si^+$) and anion ($(CH_3)_3Si^-$), respectively.

The analysis concerns the electrical characteristics of the DBD at first. The studies aim to clarify the impact of small TMS admixtures added to the carrier gas Ar on the ignition behavior as well as on the temporal evolution of discharges at conditions typical of deposition experiments. In particular, the impact of Penning ionization processes of excited argon atoms with TMS molecules is investigated since they can play a significant role for the electron production in atmospheric-pressure plasmas and can influence the ignition and burning voltage of such discharges [21, 35]. Furthermore, it is analyzed how the trimethylsilyl anions, resulting from the dissociative electron attachment to TMS, influence the discharge behavior.

Measurements of the ignition voltage of DBDs in argon with TMS admixtures of up to 200 ppm supplement these numerical studies. The total rate coefficient of collisions between excited argon atoms and TMS is determined by comparing measured and calculated ignition voltages. This comparison also provides information about the contribution of the Penning ionization and the quenching of excited argon atoms by monomer molecules, leading to the dissociation of TMS into neutral reaction products.

Secondly, model calculations for operating conditions typical of deposition experiments are presented and discussed. For these calculations, the basic reaction kinetics scheme of TMS has been extended by about 540 additional collision processes involving further 56 species. That makes it possible to also get information about the behavior of, e.g., the primary radicals trimethylsilyl ($(CH_3)_3Si$) and methyl (CH_3) as well as other radical species, further stable molecules, such as hexamethyldisilane ($(CH_3)_3SiSi(CH_3)_3$), trimethylsilane ($(CH_3)_3SiH$) or methane (CH_4) and ethane (C_2H_6), or other positive and negative charge carriers. Details of this extended reaction kinetics scheme are given, and selected results of corresponding modeling studies are represented and discussed. The analysis includes a comparison of measured and calculated discharge currents as well as a comprehensive representation of key species generated in the DBD during the residence time of the gas in the discharge area as predicted by numerical modeling. In addition, the impact of ionic species on the film deposition in plasma polymerization is discussed.

Description of the Model

The modeling studies presented in this paper are related to the plane-parallel DBD configuration used in [33] for electrical measurements. A schematic representation of the plasma reactor is shown in Fig. 1a. The DBD was ignited between two rectangular electrodes with a width of 8 cm and a length in flow direction of 1 cm corresponding to a discharge area $A = 8\,\mathrm{cm}^2$. Both electrodes were made of steel mesh glued onto borofloat glass dielectrics with a thickness Δ of 2 mm and a relative permittivity ε_r of 4.6. The gap width d was

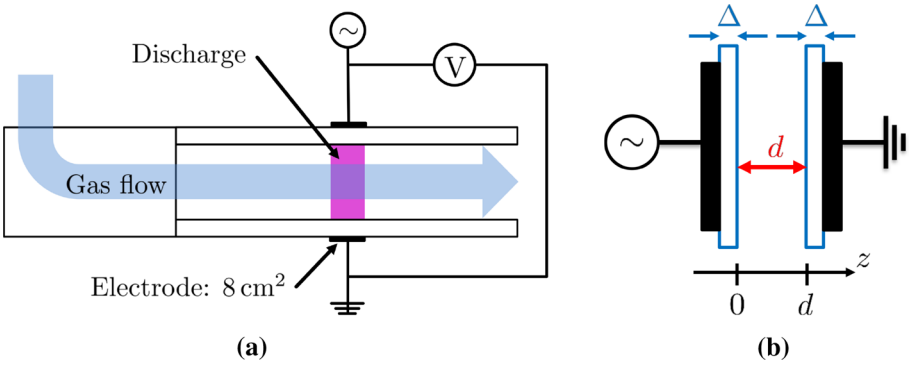

Fig. 1 Schematic drawing of the plasma reactor, **a** with the discharge area $A = 8\,\mathrm{cm}^2$ and of the spatially one-dimensional discharge geometry, **b** with gap width d and thickness of dielectric layers Δ

1 mm. A high-voltage (HV) generator was used to power the discharge by the sinusoidal voltage

$$U_a(t) = U_{a,0}\sin(2\pi ft) \tag{1}$$

with the amplitude $U_{a,0}$ at a frequency f of 86.2 kHz.

A schematic representation of the corresponding discharge geometry used in the modeling studies is displayed in Fig. 1b. The time-dependent, spatially one-dimensional model considers the axial component z of the plasma between the plane-parallel, dielectric covered electrodes, where the electrode on the left side is powered by the voltage (1) and that to the right is grounded. Such a spatially one-dimensional treatment is well suited for the analysis of DBDs operating in the homogeneous or glow mode [36] and was successfully applied for the analysis of DBDs, e.g., in Ar [34], Ar-HMDSO mixtures [35, 37], N_2 with 0.1 vol% O_2 [38], and CO_2 [39].

Basic Relations

The fluid model comprises balance equations for the densities n_j of relevant neutral particles and charge carriers as well as for the electron energy density $n_e u_e$, the Poisson equation to determine the electric potential Φ and field E, as well as a balance equation for the surface charge density σ_s to consider the accumulation of charge carriers on the dielectric surfaces at $z_0 = 0$ and $z_0 = d$. A schematic representation of the basic relations and the sequence of their solution is shown in Fig. 2. Here e_0, ε_0 and Z_j are the elementary charge, vacuum permittivity and particle charge number, respectively, E_D denotes the electric field inside the respective dielectric barrier, $\nu = -1$ at $z_0 = 0$ and $\nu = 1$ at $z_0 = d$.

The fluxes Γ_j of heavy particles are calculated in the common drift-diffusion approximation, while the particle flux Γ_e and energy flux Q_e of electrons are determined by the improved drift-diffusion approximation introduced by Becker et al. [40, 41]. S_j represents the gain and loss of particles of kind j in the plasma due to collision processes and radiative transitions, and $\tilde{S}_e$ denotes the gain and loss of electron energy caused by the various collision processes involving electrons.

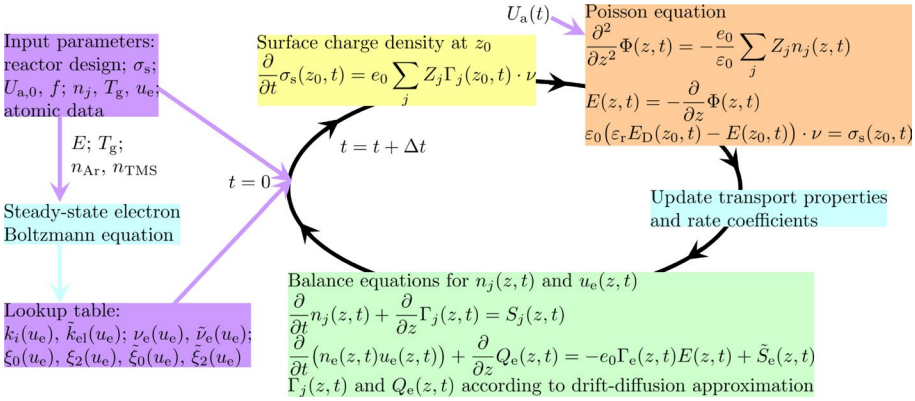

Fig. 2 Sketch of the time-dependent, spatially one-dimensional fluid model with time step size Δt

Regarding the electrons, their rate coefficients k_i of the different inelastic collision processes with heavy particles and their energy rate coefficient $\tilde{k}_{el}$ for elastic collisions were obtained by solving the steady-state, spatially homogeneous Boltzmann equation for given reduced electric field E/N with the background gas density N, gas temperature T_g, Ar-TMS mixture ratio, and atomic data, using the electron collision cross sections specified in "Reaction Kinetics Schemes" section. The solution of this electron kinetic equation was done by means of a generalized version of the solution method [42] adapted to take into account non-conservative electron collision processes [43]. It also yields the dissipation frequencies ν_e and $\tilde{\nu}_e$ as well as the transport coefficients ξ_0, ξ_2, $\tilde{\xi}_0$, and $\tilde{\xi}_2$ of the electrons [41]. Afterwards, lookup tables for these coefficients and frequencies as a function of the mean electron energy u_e were generated for the respective mixture ratio of Ar and TMS and were used in the fluid model calculations. Further details about the basic relations, the boundary conditions and the solution method are given in [35]. In particular, flux boundary conditions are employed at the dielectric surfaces when solving the particle balance equations, where stable molecules related to the TMS kinetics are assumed to be completely reflected while radical species are not reflected. That is, the latter stick and/or recombine on the surface [20, 44].

Reaction Kinetics Schemes

The reaction kinetics for Ar-TMS mixtures is based on the argon model reported in [34]. The reaction kinetics scheme for argon takes into account ground state argon atoms (Ar[1p$_0$] in Paschen notation), metastable (Ar[1s$_5$] and Ar[1s$_3$]) and resonance (Ar[1s$_4$] and Ar[1s$_2$]) atoms, lumped excited states Ar[2p] and Ar[2p′], a summarized higher excited atomic level Ar[hl], excimers $Ar_2[^3\Sigma_u^+, v = 0]$, $Ar_2[^1\Sigma_u^+, v = 0]$, $Ar_2[^3\Sigma_u^+, v \gg 0]$ and $Ar_2[^1\Sigma_u^+, v \gg 0]$ in the vibrational ground ($v = 0$) and highly vibrationally excited ($v \gg 0$) states with the energy levels 9.76 eV, 9.84 eV, 11.37 eV and 11.45 eV, respectively, as well as the atomic (Ar^+) and molecular (Ar_2^+) ion. These 14 heavy particle components and the electrons are subject to 114 reactions including 70 electron collision processes, 24 heavy particle collision processes, and 20 radiative transitions. This argon model was extended by including relevant collision processes for small amounts of the precursor gas TMS. Following [35], the electrical characteristics of atmospheric-pressure DBDs in argon with small

monomer admixtures can be determined by the collision processes of TMS with electrons and argon species as well as of the primary ions generated. This basic reaction kinetics model related to TMS is listed in Table 1.

The electron collision processes of TMS include elastic collisions, two vibrational excitations with the energy losses 0.11 and 0.27 eV, a total electronic excitation with the energy loss 7.45 eV, leading to the dissociation into the trimethylsilyl and the methyl radical [20], a total ionization with the energy loss 9.8 eV, resulting in the trimethylsilyl cation and a methyl radical, as well as the dissociative electron attachment, leading to the formation of

Table 1 Collision processes related to TMS included in the basic reaction kinetics model in addition to the argon model reported in [34]

Index	Reaction	Rate coefficient	References
Elastic electron collisions			
1	$(CH_3)_4Si + e \rightarrow (CH_3)_4Si + e$	$f(u_e)$	[45]
Electron impact excitation and dissociation			
2	$(CH_3)_4Si + e \rightarrow (CH_3)_4Si[v_1] + e$	$f(u_e)$	[45]
3	$(CH_3)_4Si + e \rightarrow (CH_3)_4Si[v_2] + e$	$f(u_e)$	[45]
4	$(CH_3)_4Si + e \rightarrow (CH_3)_3Si + CH_3 + e$	$f(u_e)$	[20, 45]
Electron impact ionization and detachment			
5	$(CH_3)_4Si + e \rightarrow (CH_3)_3Si^+ + CH_3 + 2e$	$f(u_e)$	[46]
6	$(CH_3)_3Si^- + e \rightarrow (CH_3)_3Si + 2e$	$f(u_e)$	[47–49]
Dissociative electron attachment			
7	$(CH_3)_4Si + e \rightarrow (CH_3)_3Si^- + CH_3$	$f(u_e)$	[45]
Ion-molecule reactions			
8	$Ar^+ + (CH_3)_4Si \rightarrow (CH_3)_3Si^+ + CH_3 + Ar[1p_0]$	1.5×10^{-15}	[36, 50]
9	$Ar_2^+ + (CH_3)_4Si \rightarrow (CH_3)_3Si^+ + CH_3 + 2\,Ar[1p_0]$	1.2×10^{-15}	[36, 50]
Quenching of excited argon species leading to Penning ionization			
10–16	$Ar^* + (CH_3)_4Si \rightarrow (CH_3)_3Si^+ + CH_3 + Ar[1p_0] + e$	k^{Pl}_{M,Ar^*}	See text
Quenching of excited argon species leading to neutral products			
17–23	$Ar^* + (CH_3)_4Si \rightarrow (CH_3)_3Si + CH_3 + Ar[1p_0]$	k^{Q}_{M,Ar^*}	See text
24–27	$Ar_2^* + (CH_3)_4Si \rightarrow (CH_3)_3Si + CH_3 + 2\,Ar[1p_0]$	k_{M,Ar^*}	Analogous to Ar^* [51, 52]
Electron-ion recombination			
28	$(CH_3)_3Si^+ + e \rightarrow (CH_3)_2Si + CH_3$	$1.8 \times 10^{-12} \times (T_e/300)^{-0.5}$	[53, 54]; see text
Collisional detachment of electrons			
29–35	$Ar^* + (CH_3)_3Si^- \rightarrow (CH_3)_3Si + Ar[1p_0] + e$	5.9×10^{-16}	[36, 55]
36–39	$Ar_2^* + (CH_3)_3Si^- \rightarrow (CH_3)_3Si + 2\,Ar[1p_0] + e$	5.9×10^{-16}	[36, 55]
Ion-ion recombination			
40	$Ar^+ + (CH_3)_3Si^- \rightarrow (CH_3)_3Si + Ar[hl]$	1.1×10^{-13}	[56]
41	$Ar_2^+ + (CH_3)_3Si^- \rightarrow (CH_3)_3Si + Ar[2p'] + Ar[1p_0]$	8.7×10^{-14}	[56]
42	$(CH_3)_3Si^+ + (CH_3)_3Si^- \rightarrow 2\,(CH_3)_3Si$	8.9×10^{-14}	[56]

The rate coefficients are given in m^3/s. Rate coefficients $f(u_e)$ are obtained from the solution of the electron Boltzmann equation as a function of the mean electron energy u_e using the cross section data of the reference given. $T_e = 2u_e/(3k_B)$ is the electron temperature in K, and $T_g = 300$ K. Ar^* denotes $Ar[1s_{5..2}]$, Ar[2p], $Ar[2p']$, and Ar[hl] as well as Ar_2^* abbreviates $Ar_2[^3\Sigma_u^+, v = 0]$, $Ar_2[^1\Sigma_u^+, v = 0]$, $Ar_2[^3\Sigma_u^+, v \gg 0]$, and $Ar_2[^1\Sigma_u^+, v \gg 0]$

the trimethylsilyl anion and CH_3. The corresponding electron collision cross sections are given in [45, 46].

Furthermore, collision processes of TMS with atomic and molecular argon ions as well as with excited argon atoms and molecules are taken into account. Here, the Langevin capture rate coefficient [36] is used for ion-molecule reactions, where the polarizability of TMS is $11.04 \times 10^{-30}\,\mathrm{m}^3$ [50].

Regarding collision processes of TMS with excited argon atoms and molecules, the information in the literature is diverse. Experimental investigations on TMS dissociation processes in plasmas provide rate coefficients $k_{\mathrm{M,Ar^*}}$ for the reaction of the monomer with the metastable atom $\mathrm{Ar}[1s_5]$ ranging from 6.0×10^{-18} to $2.2 \times 10^{-17}\,\mathrm{m}^3/\mathrm{s}$ [57]. When comparing these values with those for collisions of excited argon atoms with several atoms and molecules reported in [51] and that for $\mathrm{Ar}[1s_5]$ collisions with HMDSO [58], the rate coefficient $k_{\mathrm{M,Ar^*}}$ is expected to be larger by a factor of 10 at least. In particular, when using the hard sphere cross section approach with a collision radius of $2.725 \times 10^{-10}\,\mathrm{m}$ for $\mathrm{Ar}[1s_5]$ [51] and the van-der-Waals radius for TMS [50] of $2.92 \times 10^{-10}\,\mathrm{m}$, a rate coefficient $k_{\mathrm{M,Ar^*}}$ of about $5 \times 10^{-16}\,\mathrm{m}^3/\mathrm{s}$ results. Furthermore, Jauberteau et al. [57] state that collisions of $\mathrm{Ar}[1s_5]$ with TMS mainly lead to the formation of neutral radicals. However, Penning ionization should take place, because the energy of excited argon atoms is large enough to ionize TMS. In particular, the fraction α_{Pl} leading to Penning ionization was measured to be 0.06 for collisions of argon metastables with TMS and 0.5 for collisions of argon metastables with trimethylsilane ($(CH_3)_3SiH$) in [59].

In order to clarify this situation, the determination of the rate coefficient $k_{\mathrm{M,Ar^*}}$ and the Penning ionization fraction α_{Pl} with $0 \leq \alpha_{\mathrm{Pl}} \leq 1$ as well as an analysis of their impact on modeling results are part of the present studies. Thus, the Penning ionization reaction

$$\mathrm{Ar^*} + (CH_3)_4Si \xrightarrow{k^{\mathrm{Pl}}_{\mathrm{M,Ar^*}}} (CH_3)_3Si^+ + CH_3 + \mathrm{Ar}[1p_0] + \mathrm{e} \tag{2}$$

with the rate coefficient $k^{\mathrm{Pl}}_{\mathrm{M,Ar^*}} = \alpha_{\mathrm{Pl}} k_{\mathrm{M,Ar^*}}$ and the quenching process

$$\mathrm{Ar^*} + (CH_3)_4Si \xrightarrow{k^{\mathrm{Q}}_{\mathrm{M,Ar^*}}} (CH_3)_3Si + CH_3 + \mathrm{Ar}[1p_0] \tag{3}$$

with the rate coefficient $k^{\mathrm{Q}}_{\mathrm{M,Ar^*}} = (1 - \alpha_{\mathrm{Pl}}) k_{\mathrm{M,Ar^*}}$ are considered in the reaction kinetics scheme for every excited atomic species, abbreviated by $\mathrm{Ar^*}$. In reaction (2), the TMS molecule is dissociated into a trimethylsilyl ion, a methyl radical and an electron, which gets most of the excess energy, and the quenching process (3) results in a trimethylsilyl and a methyl radical. In addition, the quenching of TMS by argon excimers is considered leading to the formation of trimethylsilyl, methyl and two argon ground state atoms. Following [52], the corresponding rate coefficient is assumed to equal the rate coefficient $k_{\mathrm{M,Ar^*}}$ for reactions of the monomer with excited argon atoms.

Reactions of the trimethylsilyl cation $(CH_3)_3Si^+$ comprise the electron-ion recombination and the ion-ion mutual neutralization due to the interaction with $(CH_3)_3Si^-$. The recombination of $(CH_3)_3Si^+$ by electron impact leads to the formation of a dimethylsilylene ($(CH_3)_2Si$) and a methyl radical [60]. The corresponding thermal reaction rate coefficient at 300 K is assumed to be similar to that of the HMDSO cation given in [53] and the dependence on the electron temperature $T_e = 2u_e/(3k_B)$ with the Boltzmann constant k_B is approximated according to [54]. The rate coefficients for the mutual neutralization of the negative trimethylsilyl ion $(CH_3)_3Si^-$ due to interaction with the positive ions Ar^+, Ar_2^+, and $(CH_3)_3Si^+$ were derived from the approximate scaling formula

proposed by Hickman [56]. The electron impact detachment cross section of $(CH_3)_3Si^-$ with an energy loss of 0.971 eV [61] was obtained by scaling from the classical ionization model of Thomson [62] as discussed in [47, 63] using the cross sections for detachment from H^- for energies $U < 10\,\text{eV}$ and from C^- for larger energies given in [48, 49]. Furthermore, detachment processes of $(CH_3)_3Si^-$ due to collisions with excited argon atoms and molecules are taken into account. The corresponding rate coefficient was estimated by means of the Langevin formula for ion-molecule reactions [36], using the polarizability of argon of $1.64 \times 10^{-30}\,\text{m}^3$ [55]. Moreover, the mobilities of the trimethylsilyl ions times background gas density were estimated by use of the polarization mobility [64] obtained from the Langevin theory and amount to $5.7 \times 10^{21}\,(\text{V m s})^{-1}$ for the gas mixtures under consideration. The corresponding diffusion coefficient was calculated using Einstein's relation [36].

The reaction kinetics set in Table 1 does not provide information about the spatio-temporal behavior of the radicals trimethylsilyl ($(CH_3)_3Si$), dimethylsilylene ($(CH_3)_2Si$), and methyl (CH_3) as well as other neutral species and charge carriers. Further collision processes, which are included in an extended reaction kinetics scheme related to TMS, are given Table 2. This extended set of reactions takes into account the collision processes of the neutral species listed in Table 3 and ions given in Table 4. Table 3 also specifies the masses, enthalpies of formation, electron affinities, ionization potentials, and polarizabilities of the neutral species.

Regarding the electron impact ionization processes of the organosilicon species in Table 2, collision cross sections were calculated by application of the modified additivity rule of Deutsch et al. [65], using the collision cross sections for carbon [66], hydrogen [67], and silicon [68, 69]. The electron-impact cross sections of various hydrocarbons and hydrogen- or carbon-containing species leading to ionization, attachment or dissociation as well as the electron detachment cross sections of H^- and CH_2^- were taken from the literature given in Table 2. The rate coefficients of most ion-molecule reactions were determined by Langevin formula [36] using the polarizabilities given in Table 3.

Collision processes of excited argon atoms and molecules with different neutral species can lead to dissociation into neutral fragments and/or to Penning ionization. The rate coefficients and the fraction of dissociation or Penning ionization for the collision processes of the organosilicon species were estimated in accordance with the collision processes of TMS or HMDSO. For the corresponding reactions with hydrocarbons or hydrogen molecules the rate coefficients provided by the references given in Table 2 were employed in general.

The rate coefficients of the electron recombination due to collisions with organosilicon ions were estimated to have a typical value of $1.0 \times 10^{-12}\text{m}^3/\text{s}$ at $T_e = 300\,\text{K}$ with a dependence on T_e approximated according to [54]. The corresponding rate coefficients and branching ratios for the hydrocarbon ions and H_2^+ were generally taken from the literature.

Except for the H^+–H^- reaction, the rate coefficients of the ion-ion recombination processes were calculated by means of the scaling formula given by Hickman [56]. The compilation of neutral-neutral reactions at the end of Table 2 includes collision processes with two-body rate coefficients larger than $1.0 \times 10^{-18}\text{m}^3/\text{s}$ only, where the rate coefficients originate from the references given in Table 2. Notice that collision processes of the 16 neutral reaction products pentamethyl[(trimethylsilyl)methyl]disilane, octamethyltrisilane, 1,1,1,2,2,3,3-heptamethyltrisilane, bis(trimethylsilyl)methane, ethylpentamethyldisilane, 1,1,2,2-tetramethyldisilane, 1,3-dimethyl-1,3-disilabicyclo[1.1.0]butane, ethyltrimethylsilane, 1,1-dimethylsilirane, 1,1-dimethylsilirene, ethynylsilane, n-butane, 1-butene, 1,3-butadiene, propane, and propene specified in Table 3 are neglected.

Table 2 Further collision processes related to TMS included in the extended reaction kinetics model in addition to the collision processes in Table 1 and the argon model reported in [34]

Index	Reaction	Rate coefficient	References
Electron impact ionization and detachment			
43	$(CH_3)_3Si + e \rightarrow (CH_3)_3Si^+ + 2e$	$f(u_e)$	[65–69]
44	$(CH_3)_2Si + e \rightarrow (CH_3)_2Si^+ + 2e$	$f(u_e)$	[65–69]
45	$(CH_3)_3SiSi(CH_3)_3 + e \rightarrow (CH_3)_3Si^+ + (CH_3)_3Si + 2e$	$f(u_e)$	[65–69]
46	$(CH_3)_3SiH + e \rightarrow (CH_3)_2SiH^+ + CH_3 + 2e$	$f(u_e)$	[65–69] ×2/3 [70]
47	$(CH_3)_3SiH + e \rightarrow (CH_3)_3Si^+ + H + 2e$	$f(u_e)$	[65–69] ×1/3 [70]
48	$`(CH_3)_2SiCH_2 + e \rightarrow (CH_3)_2SiCH_2^+ + 2e$	$f(u_e)$	[65–69]
49	$(CH_3)_2SiH_2 + e \rightarrow (CH_3)_2SiH^+ + H + 2e$	$f(u_e)$	[65–69]
50	$(CH_3)_2SiH + e \rightarrow (CH_3)_2Si^+ + H + 2e$	$f(u_e)$	[65–69]
51	$CH_3Si + e \rightarrow CH_3Si^+ + 2e$	$f(u_e)$	[65–69]
52	$(CH_3)_2Si\langle \begin{smallmatrix} CH_2 \\ CH_2 \end{smallmatrix} \rangle Si(CH_3)_2 + e \rightarrow (CH_3)_2Si\langle \begin{smallmatrix} CH_2 \\ CH_2 \end{smallmatrix} \rangle Si^+CH_3 + CH_3 + 2e$	$f(u_e)$	[65–69]
53	$(CH_3)_3SiSiH(CH_3)_2 + e \rightarrow (CH_3)_3Si^+ + (CH_3)_2SiH + 2e$	$f(u_e)$	[65–69]
54	$CH_3 + e \rightarrow CH_3^+ + 2e$	$f(u_e)$	[71]
55	$CH_4 + e \rightarrow CH_4^+ + 2e$	$f(u_e)$	[72]
56	$CH_4 + e \rightarrow CH_3^+ + H + 2e$	$f(u_e)$	[72]
57	$CH_4 + e \rightarrow CH_2^+ + H_2 + 2e$	$f(u_e)$	[72]
58	$CH_4 + e \rightarrow CH^+ + H_2 + H + 2e$	$f(u_e)$	[72]
59	$CH_4 + e \rightarrow C^+ + 2H_2 + 2e$	$f(u_e)$	[72]
60	$CH_4 + e \rightarrow H_2^+ + CH_2 + 2e$	$f(u_e)$	[72]
61	$CH_4 + e \rightarrow H^+ + CH_3 + 2e$	$f(u_e)$	[72]
62	$CH_2 + e \rightarrow CH_2^+ + 2e$	$f(u_e)$	[71]
63	$CH + e \rightarrow CH^+ + 2e$	$f(u_e)$	[73]
64	$C_2H_6 + e \rightarrow C_2H_6^+ + 2e$	$f(u_e)$	[74]
65	$C_2H_6 + e \rightarrow C_2H_5^+ + H + 2e$	$f(u_e)$	[74]

Table 2 (continued)

Index	Reaction	Rate coefficient	References
66	$C_2H_6 + e \rightarrow C_2H_4^+ + H_2 + 2e$	$f(u_e)$	[74]
67	$C_2H_6 + e \rightarrow C_2H_3^+ + H + H_2 + 2e$	$f(u_e)$	[74]
68	$C_2H_6 + e \rightarrow C_2H_2^+ + 2H_2 + 2e$	$f(u_e)$	[74]
69	$C_2H_6 + e \rightarrow CH_3^+ + CH_3 + 2e$	$f(u_e)$	[74]
70	$C_2H_4 + e \rightarrow C_2H_4^+ + 2e$	$f(u_e)$	[75]
71	$C_2H_2 + e \rightarrow C_2H_2^+ + 2e$	$f(u_e)$	[76]
72	$H_2 + e \rightarrow H_2^+ + 2e$	$f(u_e)$	[77]
73	$H_2 + e \rightarrow H^+ + H + 2e$	$f(u_e)$	[77]
74	$H + e \rightarrow H^+ + 2e$	$f(u_e)$	[67]
75	$C + e \rightarrow C^+ + 2e$	$f(u_e)$	[66]
76	$H^- + e \rightarrow H + 2e$	$f(u_e)$	[48, 78]
77	$CH_2^- + e \rightarrow CH_2 + 2e$	$f(u_e)$	[47–49]
Dissociative electron attachment			
78	$CH_4 + e \rightarrow CH_3 + H^-$	$f(u_e)$	[79, 80]
79	$CH_4 + e \rightarrow H_2 + CH_2^-$	$f(u_e)$	[79, 80]
80	$C_2H_6 + e \rightarrow C_2H_5 + H^-$	$f(u_e)$	[81]
81	$C_2H_4 + e \rightarrow C_2H_3 + H^-$	$f(u_e)$	[82]
82	$C_2H_2 + e \rightarrow C_2H + H^-$	$f(u_e)$	[76, 83]
83	$H_2 + e \rightarrow H + H^-$	$f(u_e)$	[77]
Electron impact dissociation			
84	$CH_3 + e \rightarrow CH_2 + H + e$	$f(u_e)$	[84]
85	$CH_4 + e \rightarrow CH_3 + H + e$	$f(u_e)$	[85, 86]
86	$CH_4 + e \rightarrow CH_2 + H_2 + e$	$f(u_e)$	[85, 86]
87	$CH_2 + e \rightarrow CH + H + e$	$f(u_e)$	[84]
88	$CH + e \rightarrow C + H + e$	$f(u_e)$	[84]

Table 2 (continued)

Index	Reaction	Rate coefficient	References
89	$C_2H_6 + e \rightarrow C_2H_4 + H_2 + e$	$f(u_e)$	[81]
90	$C_2H_4 + e \rightarrow C_2H_2 + H_2 + e$	$f(u_e)$	[87]
91	$C_2H_2 + e \rightarrow C_2H + H + e$	$f(u_e)$	[87]
92	$H_2 + e \rightarrow 2H + e$	$f(u_e)$	[77]
Ion-molecule reactions			
93	$Ar^+ + (CH_3)_3Si \rightarrow (CH_3)_3Si^+ + Ar[1p_0]$	1.4×10^{-15}	[36, 50]
94	$Ar_2^+ + (CH_3)_3Si \rightarrow (CH_3)_3Si^+ + 2Ar[1p_0]$	1.1×10^{-15}	[36, 50]
95	$Ar^+ + (CH_3)_2Si \rightarrow (CH_3)_2Si^+ + Ar[1p_0]$	1.2×10^{-15}	[36, 50]
96	$Ar_2^+ + (CH_3)_2Si \rightarrow (CH_3)_2Si^+ + 2Ar[1p_0]$	1.0×10^{-15}	[36, 50]
97	$Ar^+ + (CH_3)_3SiSi(CH_3)_3 \rightarrow (CH_3)_3Si^+ + (CH_3)_3Si + Ar[1p_0]$	1.8×10^{-15}	[36, 50]
98	$Ar_2^+ + (CH_3)_3SiSi(CH_3)_3 \rightarrow (CH_3)_3Si^+ + (CH_3)_3Si + 2Ar[1p_0]$	1.4×10^{-15}	[36, 50]
99	$Ar^+ + (CH_3)_3SiH \rightarrow (CH_3)_3Si^+ + H + Ar[1p_0]$	1.4×10^{-15}	[36, 50]
100	$Ar_2^+ + (CH_3)_3SiH \rightarrow (CH_3)_3Si^+ + H + 2Ar[1p_0]$	1.1×10^{-15}	[36, 50]
101	$Ar^+ + (CH_3)_2SiCH_2 \rightarrow (CH_3)_2Si^+ + CH_2 + Ar[1p_0]$	1.4×10^{-15}	[36, 50]
102	$Ar_2^+ + (CH_3)_2SiCH_2 \rightarrow (CH_3)_2Si^+ + CH_2 + 2Ar[1p_0]$	1.1×10^{-15}	[36, 50]
103	$Ar^+ + (CH_3)_2SiH_2 \rightarrow (CH_3)_2SiH^+ + H + Ar[1p_0]$	1.3×10^{-15}	[36, 50]
104	$Ar_2^+ + (CH_3)_2SiH_2 \rightarrow (CH_3)_2SiH^+ + H + 2Ar[1p_0]$	1.1×10^{-15}	[36, 50]
105	$Ar^+ + (CH_3)_2SiH \rightarrow (CH_3)_2SiH^+ + Ar[1p_0]$	1.3×10^{-15}	[36, 50]
106	$Ar_2^+ + (CH_3)_2SiH \rightarrow (CH_3)_2SiH^+ + 2Ar[1p_0]$	1.1×10^{-15}	[36, 50]
107	$Ar^+ + (CH_3)Si \rightarrow (CH_3)Si^+ + Ar[1p_0]$	1.1×10^{-15}	[36, 50]
108	$Ar_2^+ + (CH_3)Si \rightarrow (CH_3)Si^+ + 2Ar[1p_0]$	9.3×10^{-16}	[36, 50]
109	$Ar^+ + (CH_3)_2Si\langle \begin{smallmatrix} CH_2 \\ CH_2 \end{smallmatrix} \rangle Si(CH_3)_2 \rightarrow (CH_3)_2Si\langle \begin{smallmatrix} CH_2 \\ CH_2 \end{smallmatrix} \rangle Si^+CH_3 + CH_3 + Ar[1p_0]$	1.7×10^{-15}	[36, 50]
110	$Ar_2^+ + (CH_3)_2Si\langle \begin{smallmatrix} CH_2 \\ CH_2 \end{smallmatrix} \rangle Si(CH_3)_2 \rightarrow (CH_3)_2Si\langle \begin{smallmatrix} CH_2 \\ CH_2 \end{smallmatrix} \rangle Si^+CH_3 + CH_3 + 2Ar[1p_0]$	1.3×10^{-15}	[36, 50]

Table 2 (continued)

Index	Reaction	Rate coefficient	References
111	$Ar^+ + (CH_3)_3SiSiH(CH_3)_2 \rightarrow (CH_3)_3Si^+ + (CH_3)_2SiH + Ar[1p_0]$	1.7×10^{-15}	[36, 50]
112	$Ar_2^+ + (CH_3)_3SiSiH(CH_3)_2 \rightarrow (CH_3)_3Si^+ + (CH_3)_2SiH + 2Ar[1p_0]$	1.3×10^{-15}	[36, 50]
113	$Ar^+ + CH_3 \rightarrow CH_3^+ + Ar[1p_0]$	1.1×10^{-15}	[36, 50]
114	$Ar_2^+ + CH_3 \rightarrow CH_3^+ + 2Ar[1p_0]$	1.0×10^{-15}	[36, 50]
115	$Ar^+ + CH_4 \rightarrow CH_4^+ + Ar[1p_0]$	8.2×10^{-17}	[88]
116	$Ar^+ + CH_4 \rightarrow CH_3^+ + H + Ar[1p_0]$	6.48×10^{-16}	[88]
117	$Ar^+ + CH_4 \rightarrow CH_2^+ + H_2 + Ar[1p_0]$	9.0×10^{-17}	[88]
118	$Ar_2^+ + CH_4 \rightarrow CH_4^+ + 2Ar[1p_0]$	9.3×10^{-16}	[88]
119	$Ar^+ + CH_2 \rightarrow CH_2^+ + Ar[1p_0]$	1.0×10^{-15}	[36, 50]
120	$Ar_2^+ + CH_2 \rightarrow CH_2^+ + 2Ar[1p_0]$	1.0×10^{-15}	[36, 50]
121	$Ar^+ + CH \rightarrow CH^+ + Ar[1p_0]$	1.1×10^{-15}	[36, 50]
122	$Ar_2^+ + CH \rightarrow CH^+ + 2Ar[1p_0]$	1.0×10^{-15}	[36, 50]
123	$Ar^+ + C \rightarrow C^+ + Ar[1p_0]$	1.0×10^{-15}	[36, 50]
124	$Ar_2^+ + C \rightarrow C^+ + 2Ar[1p_0]$	1.0×10^{-15}	[36, 50]
125	$Ar^+ + C_2H_6 \rightarrow C_2H_5^+ + H + Ar[1p_0]$	2.05×10^{-16}	[89]
126	$Ar^+ + C_2H_6 \rightarrow C_2H_4^+ + H_2 + Ar[1p_0]$	2.05×10^{-16}	[89]
127	$Ar^+ + C_2H_6 \rightarrow C_2H_3^+ + H_2 + H + Ar[1p_0]$	4.33×10^{-16}	[89]
128	$Ar^+ + C_2H_6 \rightarrow C_2H_2^+ + 2H_2 + Ar[1p_0]$	2.28×10^{-16}	[89]
129	$Ar^+ + C_2H_6 \rightarrow CH_3^+ + CH_3 + Ar[1p_0]$	6.9×10^{-17}	[89]
130	$Ar_2^+ + C_2H_6 \rightarrow C_2H_5^+ + H + 2Ar[1p_0]$	1.7×10^{-16}	[89]
131	$Ar_2^+ + C_2H_6 \rightarrow C_2H_4^+ + H_2 + 2Ar[1p_0]$	5.4×10^{-16}	[89]
132	$Ar^+ + C_2H_4 \rightarrow C_2H_4^+ + Ar[1p_0]$	4.4×10^{-17}	[90]
133	$Ar^+ + C_2H_4 \rightarrow C_2H_3^+ + H + Ar[1p_0]$	8.4×10^{-16}	[90]
134	$Ar^+ + C_2H_4 \rightarrow C_2H_2^+ + H_2 + Ar[1p_0]$	2.2×10^{-16}	[90]

Table 2 (continued)

Index	Reaction	Rate coefficient	References
135	$Ar_2^+ + C_2H_4 \rightarrow C_2H_3^+ + H + 2Ar[1p_0]$	1.1×10^{-15}	[36, 50]
136	$Ar^+ + C_2H_2 \rightarrow C_2H_2^+ + Ar[1p_0]$	4.2×10^{-16}	[90]
137	$Ar_2^+ + C_2H_2 \rightarrow C_2H_2^+ + 2Ar[1p_0]$	9.6×10^{-16}	[36, 50]
138	$Ar^+ + H_2 \rightarrow ArH^+ + H$	1.0×10^{-15}	[91]
139	$Ar_2^+ + H_2 \rightarrow Ar_2H^+ + H$	4.9×10^{-16}	[92]
140	$Ar^+ + H \rightarrow H^+ + Ar[1p_0]$	1.9×10^{-15}	[15, 36]
141	$Ar_2^+ + H \rightarrow H^+ + 2Ar[1p_0]$	1.9×10^{-15}	[15, 36]
142	$(CH_3)_3Si^+ + (CH_3)_2Si\langle \begin{smallmatrix} CH_2 \\ CH_2 \end{smallmatrix} \rangle Si(CH_3)_2 \rightarrow (CH_3)_2Si\langle \begin{smallmatrix} CH_2 \\ CH_2 \end{smallmatrix} \rangle Si^+CH_3 + (CH_3)_4Si$	1.4×10^{-15}	[36, 50]
143	$CH_3^+ + (CH_3)_4Si \rightarrow (CH_3)_3Si^+ + C_2H_6$	2.2×10^{-15}	[36, 50]
144	$CH_3^+ + (CH_3)_3Si \rightarrow (CH_3)_3Si^+ + CH_3$	2.0×10^{-15}	[36, 50]
145	$CH_3^+ + (CH_3)_2Si \rightarrow (CH_3)_2Si^+ + CH_3$	1.7×10^{-15}	[36, 50]
146	$CH_3^+ + (CH_3)_3SiSi(CH_3)_3 \rightarrow (CH_3)_3Si^+ + (CH_3)_3Si + CH_3$	2.7×10^{-15}	[36, 50]
147	$CH_3^+ + (CH_3)_3SiH \rightarrow (CH_3)_3Si^+ + CH_4$	2.0×10^{-15}	[36, 50]
148	$CH_3^+ + (CH_3)_2SiCH_2 \rightarrow (CH_3)_3Si^+ + CH_2$	2.0×10^{-15}	[36, 50]
149	$CH_3^+ + (CH_3)_2SiH \rightarrow (CH_3)_3Si^+ + H$	1.8×10^{-15}	[36, 50]
150	$CH_3^+ + (CH_3)_2Si\langle \begin{smallmatrix} CH_2 \\ CH_2 \end{smallmatrix} \rangle Si(CH_3)_2 \rightarrow (CH_3)_2Si\langle \begin{smallmatrix} CH_2 \\ CH_2 \end{smallmatrix} \rangle Si^+CH_3 + C_2H_6$	2.6×10^{-15}	[36, 50]
151	$(CH_3)_2Si^+ + (CH_3)_4Si \rightarrow (CH_3)_3Si^+ + (CH_3)_3Si$	1.3×10^{-15}	[36, 50]
152	$(CH_3)_2Si^+ + (CH_3)_3Si \rightarrow (CH_3)_3Si^+ + (CH_3)_2Si$	1.2×10^{-15}	[36, 50]
153	$(CH_3)_2Si^+ + (CH_3)_3SiSi(CH_3)_3 \rightarrow (CH_3)_3Si^+ + (CH_3)_3Si + (CH_3)_2Si$	1.5×10^{-15}	[36, 50]
154	$(CH_3)_2Si^+ + (CH_3)_3SiH \rightarrow (CH_3)_3Si^+ + (CH_3)_2SiH$	1.2×10^{-15}	[93]
155	$(CH_3)_2Si^+ + (CH_3)_2SiCH_2 \rightarrow (CH_3)_2SiCH_2^+ + (CH_3)_2Si$	1.2×10^{-15}	[36, 50]
156	$(CH_3)_2Si^+ + (CH_3)_2Si\langle \begin{smallmatrix} CH_2 \\ CH_2 \end{smallmatrix} \rangle Si(CH_3)_2 \rightarrow (CH_3)_2Si\langle \begin{smallmatrix} CH_2 \\ CH_2 \end{smallmatrix} \rangle Si^+CH_3 + (CH_3)_3Si$	1.5×10^{-15}	[36, 50]

Table 2 (continued)

Index	Reaction	Rate coefficient	References
157	$(CH_3)_3SiH^+ + (CH_3)_4Si \rightarrow (CH_3)_3Si^+ + (CH_3)_3Si + CH_4$	1.2×10^{-15}	[36, 50]
158	$(CH_3)_3SiH^+ + (CH_3)_3Si \rightarrow (CH_3)_3Si^+ + (CH_3)_3SiH$	1.1×10^{-15}	[36, 50]
159	$(CH_3)_3SiH^+ + (CH_3)_2Si \rightarrow (CH_3)_3Si^+ + (CH_3)_2SiH$	1.1×10^{-15}	[36, 50]
160	$(CH_3)_3SiH^+ + CH_3 \rightarrow (CH_3)_3Si^+ + CH_4$	1.0×10^{-15}	[36, 50]
161	$(CH_3)_2SiCH_2^+ + (CH_3)_3Si \rightarrow (CH_3)_3Si^+ + (CH_3)_2SiCH_2$	1.2×10^{-15}	[36, 50]
162	$(CH_3)_2SiCH_2^+ + (CH_3)_3SiH \rightarrow (CH_3)_3Si^+ + (CH_3)_3Si$	1.2×10^{-15}	[36, 50]
163	$(CH_3)_2SiCH_2^+ + (CH_3)_2SiH \rightarrow (CH_3)_3Si^+ + (CH_3)_2Si$	1.1×10^{-15}	[36, 50]
164	$(CH_3)_2SiH^+ + (CH_3)_3SiH \rightarrow (CH_3)_3Si^+ + (CH_3)_2SiH_2$	6.9×10^{-16}	[70]
165	$(CH_3)_2SiH^+ + CH_3 \rightarrow (CH_3)_3Si^+ + H$	1.1×10^{-15}	[36, 50]
166	$(CH_3)SiH_2^+ + (CH_3)_4Si \rightarrow (CH_3)_3Si^+ + H_2 + C_2H_6$	2.5×10^{-17}	[93]
167	$(CH_3)Si^+ + (CH_3)_4Si \rightarrow (CH_3)_3Si^+ + (CH_3)_2Si$	1.4×10^{-15}	[36, 50]
168	$(CH_3)_2Si\langle \begin{matrix} CH_2 \\ CH_2 \end{matrix} \rangle Si^+CH_3 + (CH_3)_2Si \rightarrow (CH_3)_3Si^+ + (CH_3)Si\langle \begin{matrix} CH_2 \\ CH_2 \end{matrix} \rangle Si(CH_3)$	9.5×10^{-16}	[36, 50]
169	$C_2H_6^+ + (CH_3)_4Si \rightarrow (CH_3)_3Si^+ + CH_3 + C_2H_6$	1.6×10^{-15}	[36, 50]
170	$C_2H_5^+ + (CH_3)_4Si \rightarrow (CH_3)_3Si^+ + C_3H_8$	1.7×10^{-15}	[36, 50]
171	$C_2H_4^+ + (CH_3)_4Si \rightarrow (CH_3)_3Si^+ + CH_3 + C_2H_4$	1.7×10^{-15}	[36, 50]
172	$C_2H_3^+ + (CH_3)_4Si \rightarrow (CH_3)_3Si^+ + C_3H_6$	1.7×10^{-15}	[36, 50]
173	$C_2H_2^+ + (CH_3)_4Si \rightarrow (CH_3)_3Si^+ + CH_3 + C_2H_2$	1.7×10^{-15}	[36, 50]
174	$CH_4^+ + (CH_3)_4Si \rightarrow (CH_3)_3Si^+ + CH_3 + CH_4$	2.1×10^{-15}	[36, 50]
175	$CH_2^+ + (CH_3)_4Si \rightarrow (CH_3)_3Si^+ + C_2H_5$	2.2×10^{-15}	[36, 50]
176	$CH^+ + (CH_3)_4Si \rightarrow (CH_3)_3Si^+ + C_2H_4$	2.3×10^{-15}	[36, 50]
177	$C^+ + (CH_3)_4Si \rightarrow (CH_3)_3Si^+ + C_2H_3$	2.4×10^{-15}	[36, 50]
178	$H_2^+ + Ar[1p_0] \rightarrow ArH^+ + H$	1.7×10^{-15}	[94]
178	$H_2^+ + (CH_3)_4Si \rightarrow (CH_3)_3Si^+ + CH_3 + H_2$	5.5×10^{-15}	[36, 50]

Table 2 (continued)

Index	Reaction	Rate coefficient	References
179	$H^+ + (CH_3)_4Si \rightarrow (CH_3)_3Si^+ + CH_4$	7.8×10^{-15}	[36, 50]
180	$ArH^+ + (CH_3)_4Si \rightarrow (CH_3)_3Si^+ + CH_4 + Ar[1p_0]$	1.5×10^{-15}	[36, 50]
181	$Ar_2H^+ + (CH_3)_4Si \rightarrow (CH_3)_3Si^+ + CH_4 + 2Ar[1p_0]$	1.2×10^{-15}	[36, 50]
Quenching of excited argon species leading to Penning ionization			
182–188	$Ar^* + (CH_3)_3Si \rightarrow (CH_3)_3Si^+ + Ar[1p_0] + e$	k_{M,Ar^*}	Analogous to $(CH_3)_4Si$
189–192	$Ar_2^* + (CH_3)_3Si \rightarrow (CH_3)_3Si^+ + 2Ar[1p_0] + e$	k_{M,Ar^*}	Analogous to $(CH_3)_4Si$
193–199	$Ar^* + (CH_3)_2Si \rightarrow (CH_3)_2Si^+ + Ar[1p_0] + e$	k_{M,Ar^*}	Analogous to $(CH_3)_4Si$
200–206	$Ar^* + (CH_3)_3SiSi(CH_3)_3 \rightarrow (CH_3)_3Si^+ + (CH_3)_3Si + Ar[1p_0] + e$	1.5×10^{-16}	Analogous to HMDSO [35]
207–213	$Ar^* + (CH_3)_3SiH \rightarrow (CH_3)_3SiH^+ + Ar[1p_0] + e$	$0.5 \times k_{M,Ar^*}$	0.5 [59] × value for $(CH_3)_4Si$
214–220	$Ar^* + (CH_3)_2SiCH_2 \rightarrow (CH_3)_2SiCH_2^+ + Ar[1p_0] + e$	k_{M,Ar^*}	Analogous to $(CH_3)_4Si$
221–224	$Ar_2^* + (CH_3)_2SiCH_2 \rightarrow (CH_3)_2SiCH_2^+ + 2Ar[1p_0] + e$	k_{M,Ar^*}	Analogous to $(CH_3)_4Si$
225–231	$Ar^* + (CH_3)_2SiH \rightarrow (CH_3)_2SiH^+ + Ar[1p_0] + e$	k_{M,Ar^*}	Analogous to $(CH_3)_4Si$
232–235	$Ar_2^* + (CH_3)_2SiH \rightarrow (CH_3)_2SiH^+ + 2Ar[1p_0] + e$	k_{M,Ar^*}	Analogous to $(CH_3)_4Si$
236–242	$Ar^* + (CH_3)SiH_2 \rightarrow (CH_3)SiH_2^+ + Ar[1p_0] + e$	k_{M,Ar^*}	Analogous to $(CH_3)_4Si$
243–246	$Ar_2^* + (CH_3)SiH_2 \rightarrow (CH_3)SiH_2^+ + 2Ar[1p_0] + e$	k_{M,Ar^*}	Analogous to $(CH_3)_4Si$
247–253	$Ar^* + (CH_3)Si \rightarrow (CH_3)Si^+ + Ar[1p_0] + e$	k_{M,Ar^*}	Analogous to $(CH_3)_4Si$
254–257	$Ar_2^* + (CH_3)Si \rightarrow (CH_3)Si^+ + 2Ar[1p_0] + e$	k_{M,Ar^*}	Analogous to $(CH_3)_4Si$
258–264	$Ar^* + (CH_3)_2Si\langle \begin{smallmatrix} CH_2 \\ CH_2 \end{smallmatrix} \rangle Si(CH_3)_2 \rightarrow (CH_3)_2Si\langle \begin{smallmatrix} CH_2 \\ CH_2 \end{smallmatrix} \rangle Si^+CH_3 + CH_3 + Ar[1p_0] + e$	1.5×10^{-16}	Analogous to HMDSO [35]
265–271	$Ar^* + (CH_3)_3SiSiH(CH_3)_2 \rightarrow (CH_3)_3Si^+ + (CH_3)_2SiH + Ar[1p_0] + e$	1.5×10^{-16}	Analogous to HMDSO [35]
272–278	$Ar^* + CH_3 \rightarrow CH_3^+ + Ar[1p_0] + e$	3.3×10^{-16}	Analogous to CH_4 [51]
279–285	$Ar^* + CH_2 \rightarrow CH_2^+ + Ar[1p_0] + e$	3.3×10^{-16}	Analogous to CH_4 [51]
286–292	$Ar^* + CH \rightarrow CH^+ + Ar[1p_0] + e$	3.3×10^{-16}	Analogous to CH_4 [51]
293–299	$Ar^* + C_2H_4 \rightarrow C_2H_4^+ + Ar[1p_0] + e$	5.3×10^{-16}	[51, 95]

Table 2 (continued)

Index	Reaction	Rate coefficient	References
300–306	$Ar^* + C_2H_2 \rightarrow C_2H_2^+ + Ar[1p_0] + e$	5.6×10^{-16}	[51, 95]
Quenching of excited argon species leading to neutral products			
307–310	$Ar_2^* + (CH_3)_2Si \rightarrow (CH_3)Si + CH_3 + 2Ar[1p_0]$	k_{M,Ar^*}	Analogous to $(CH_3)_4Si$
311–317	$Ar^* + (CH_3)_3SiSi(CH_3)_3 \rightarrow 2(CH_3)_3Si + Ar[1p_0]$	3.5×10^{-16}	Analogous to HMDSO [35]
318–321	$Ar_2^* + (CH_3)_3SiSi(CH_3)_3 \rightarrow 2(CH_3)_3Si + 2Ar[1p_0]$	5.0×10^{-16}	Analogous to HMDSO [35]
322–328	$Ar^* + (CH_3)_3SiH \rightarrow (CH_3)_2SiH + CH_3 + Ar[1p_0]$	$0.5 \times k_{M,Ar^*}$	0.5 [59] × value for $(CH_3)_4Si$
329–332	$Ar_2^* + (CH_3)_3SiH \rightarrow (CH_3)_2SiH + CH_3 + 2Ar[1p_0]$	k_{M,Ar^*}	Analogous to $(CH_3)_4Si$
333–339	$Ar^* + (CH_3)_2SiH_2 \rightarrow (CH_3)SiH_2 + CH_3 + Ar[1p_0]$	k_{M,Ar^*}	Analogous to $(CH_3)_4Si$
340–343	$Ar_2^* + (CH_3)_2SiH_2 \rightarrow (CH_3)SiH_2 + CH_3 + 2Ar[1p_0]$	k_{M,Ar^*}	Analogous to $(CH_3)_4Si$
344–350	$Ar^* + (CH_3)SiH \rightarrow Si + CH_3 + H + Ar[1p_0]$	k_{M,Ar^*}	Analogous to $(CH_3)_4Si$
351–354	$Ar_2^* + (CH_3)SiH \rightarrow Si + CH_3 + H + 2Ar[1p_0]$	k_{M,Ar^*}	Analogous to $(CH_3)_4Si$
355–361	$Ar^* + (CH_3)_2Si\langle \begin{matrix} CH_2 \\ CH_2 \end{matrix} \rangle Si(CH_3)_2 \rightarrow 2(CH_3)_2SiCH_2 + Ar[1p_0]$	3.5×10^{-16}	Analogous to HMDSO [35]
362–365	$Ar_2^* + (CH_3)_2Si\langle \begin{matrix} CH_2 \\ CH_2 \end{matrix} \rangle Si(CH_3)_2 \rightarrow 2(CH_3)_2SiCH_2 + 2Ar[1p_0]$	5.0×10^{-16}	Analogous to HMDSO [35]
366–372	$Ar^* + (CH_3)_3SiSiH(CH_3)_2 \rightarrow (CH_3)_3Si + (CH_3)_2SiH + Ar[1p_0]$	3.5×10^{-16}	Analogous to HMDSO [35]
373–376	$Ar_2^* + (CH_3)_3SiSiH(CH_3)_2 \rightarrow (CH_3)_3Si + (CH_3)_2SiH + 2Ar[1p_0]$	5.0×10^{-16}	Analogous to HMDSO [35]
377–380	$Ar_2^* + CH_3 \rightarrow CH_2 + H + 2Ar[1p_0]$	3.3×10^{-16}	Analogous to Ar^* [52]
381–387	$Ar^* + CH_4 \rightarrow CH_2 + 2H + Ar[1p_0]$	2.1×10^{-16}	[51] ×0.65 [96]
388–394	$Ar^* + CH_4 \rightarrow CH_3 + H + Ar[1p_0]$	1.2×10^{-16}	[51] ×0.35 [96]
395–398	$Ar_2^* + CH_4 \rightarrow CH_3 + H + 2Ar[1p_0]$	6.3×10^{-16}	[52]
399–402	$Ar_2^* + CH_2 \rightarrow CH + H + 2Ar[1p_0]$	3.3×10^{-16}	Analogous to CH_3
403–406	$Ar_2^* + CH \rightarrow C + H + 2Ar[1p_0]$	3.3×10^{-16}	Analogous to CH_3
407–413	$Ar^* + C_2H_6 \rightarrow C_2H_4 + 2H + Ar[1p_0]$	5.9×10^{-16}	[51] ×0.9 [96]
414–420	$Ar^* + C_2H_6 \rightarrow C_2H_5 + H + Ar[1p_0]$	0.7×10^{-16}	[51] ×0.1 [96]

Table 2 (continued)

Index	Reaction	Rate coefficient	References
421–424	$Ar_2^* + C_2H_6 \rightarrow C_2H_4 + 2H + 2Ar[1p_0]$	6.6×10^{-16}	Analogous to Ar^* [51, 52]
425–428	$Ar_2^* + C_2H_4 \rightarrow C_2H_2 + 2H + 2Ar[1p_0]$	8.1×10^{-16}	[52]
429–432	$Ar_2^* + C_2H_2 \rightarrow C_2H + H + 2Ar[1p_0]$	5.6×10^{-16}	Analogous to Ar^* [51, 52]
433–439	$Ar^* + H_2 \rightarrow 2H + Ar[1p_0]$	6.6×10^{-17}	[51]
440–443	$Ar_2^* + H_2 \rightarrow 2H + 2Ar[1p_0]$	7.6×10^{-17}	[52]
Electron-ion recombination			
444	$(CH_3)_2Si^+ + e \rightarrow (CH_3)Si + CH_3$	$1.0 \times 10^{-12} \times (T_e/300)^{-0.5}$	Estimated
445	$(CH_3)_3SiH^+ + e \rightarrow (CH_3)_2SiH + CH_3$	$1.0 \times 10^{-12} \times (T_e/300)^{-0.5}$	Estimated
446	$(CH_3)_2SiCH_2^+ + e \rightarrow (CH_3)_2Si + CH_2$	$1.0 \times 10^{-12} \times (T_e/300)^{-0.5}$	Estimated
447	$(CH_3)_2SiH^+ + e \rightarrow (CH_3)SiH + CH_3$	$1.0 \times 10^{-12} \times (T_e/300)^{-0.5}$	Estimated
448	$(CH_3)SiH_2^+ + e \rightarrow Si + CH_3 + H_2$	$1.0 \times 10^{-12} \times (T_e/300)^{-0.5}$	Estimated
449	$(CH_3)Si^+ + e \rightarrow Si + CH_3$	$1.0 \times 10^{-12} \times (T_e/300)^{-0.5}$	Estimated
450	$(CH_3)_2Si\langle \begin{matrix} CH_2 \\ CH_2 \end{matrix} \rangle Si^+CH_3 + e \rightarrow (CH_3)Si\langle \begin{matrix} CH_2 \\ CH_2 \end{matrix} \rangle Si(CH_3) + CH_3$	$1.0 \times 10^{-12} \times (T_e/300)^{-0.5}$	Estimated
451	$CH_3^+ + e \rightarrow CH_2 + H$	$2.44 \times 10^{-13} \times (T_e/300)^{-0.61}$	[97]
452	$CH_3^+ + e \rightarrow CH + 2H$	$1.39 \times 10^{-13} \times (T_e/300)^{-0.61}$	[97]
453	$CH_3^+ + e \rightarrow CH + H_2$	$7.0 \times 10^{-14} \times (T_e/300)^{-0.61}$	[97]
454	$CH_3^+ + e \rightarrow C + H_2 + H$	$2.44 \times 10^{-13} \times (T_e/300)^{-0.61}$	[97]
455	$CH_4^+ + e \rightarrow CH_3 + H$	$8.7 \times 10^{-14} \times (T_e/300)^{-0.5}$	[98, 99] ×0.25 [100]
456	$CH_4^+ + e \rightarrow CH_2 + 2H$	$2.63 \times 10^{-13} \times (T_e/300)^{-0.5}$	[98, 99] ×0.75 [100]
457	$CH_2^+ + e \rightarrow CH + H$	$2.5 \times 10^{-13} \times (T_e/300)^{-0.5}$	[98–100]
458	$C_2H_6^+ + e \rightarrow 2CH_3$	$3.7 \times 10^{-13} \times (T_e/300)^{-0.79}$	Analogous to $C_2H_5^+$ [101–103]
459	$C_2H_6^+ + e \rightarrow C_2H_5 + H$	$3.7 \times 10^{-13} \times (T_e/300)^{-0.79}$	Analogous to $C_2H_5^+$ [101–103]
460	$C_2H_5^+ + e \rightarrow CH_3 + CH_2$	$3.7 \times 10^{-13} \times (T_e/300)^{-0.79}$	[101, 102] ×0.5 [103]

Table 2 (continued)

Index	Reaction	Rate coefficient	References
461	$C_2H_5^+ + e \rightarrow C_2H_4 + H$	$3.7 \times 10^{-13} \times (T_e/300)^{-0.79}$	[101, 102] ×0.5 [103]
462	$C_2H_4^+ + e \rightarrow C_2H_3 + H$	$6.2 \times 10^{-14} \times (T_e/300)^{-0.76}$	[104]
463	$C_2H_4^+ + e \rightarrow C_2H_2 + H_2$	$3.4 \times 10^{-14} \times (T_e/300)^{-0.76}$	[104]
464	$C_2H_4^+ + e \rightarrow C_2H_2 + 2H$	$3.7 \times 10^{-13} \times (T_e/300)^{-0.76}$	[104]
465	$C_2H_4^+ + e \rightarrow C_2H + H_2 + H$	$5.6 \times 10^{-14} \times (T_e/300)^{-0.76}$	[104]
466	$C_2H_4^+ + e \rightarrow CH_4 + C$	$5.6 \times 10^{-15} \times (T_e/300)^{-0.76}$	[104]
467	$C_2H_4^+ + e \rightarrow CH_3 + CH$	$1.1 \times 10^{-14} \times (T_e/300)^{-0.76}$	[104]
468	$C_2H_4^+ + e \rightarrow CH_2 + CH_2$	$2.2 \times 10^{-14} \times (T_e/300)^{-0.76}$	[104]
469	$C_2H_3^+ + e \rightarrow C_2H_2 + H$	$1.31 \times 10^{-13} \times (T_e/300)^{-0.5}$	[98, 105] ×0.29 [106]
470	$C_2H_3^+ + e \rightarrow C_2H + H_2$	$2.7 \times 10^{-14} \times (T_e/300)^{-0.5}$	[98, 105] ×0.06 [106]
471	$C_2H_3^+ + e \rightarrow C_2H + 2H$	$2.66 \times 10^{-13} \times (T_e/300)^{-0.5}$	[98, 105] ×0.59 [106]
472	$C_2H_3^+ + e \rightarrow C_2 + H + H_2$	$1.35 \times 10^{-14} \times (T_e/300)^{-0.5}$	[98, 105] ×0.03 [106]
473	$C_2H_3^+ + e \rightarrow CH_2 + CH$	$1.35 \times 10^{-14} \times (T_e/300)^{-0.5}$	[98, 105] ×0.03 [106]
474	$C_2H_2^+ + e \rightarrow C_2H + H$	$1.35 \times 10^{-13} \times (T_e/300)^{-0.5}$	[98, 105] ×0.50 [107]
475	$C_2H_2^+ + e \rightarrow 2CH$	$3.5 \times 10^{-14} \times (T_e/300)^{-0.5}$	[98, 105] ×0.13 [107]
476	$C_2H_2^+ + e \rightarrow C_2 + 2H$	$8.1 \times 10^{-14} \times (T_e/300)^{-0.5}$	[98, 105] ×0.30 [107]
477	$C_2H_2^+ + e \rightarrow CH_2 + C$	$1.4 \times 10^{-14} \times (T_e/300)^{-0.5}$	[98, 105] ×0.05 [107]
478	$C_2H_2^+ + e \rightarrow C_2 + H_2$	$5.0 \times 10^{-15} \times (T_e/300)^{-0.5}$	[98, 105] ×0.02 [107]
479	$CH^+ + e \rightarrow C + H$	$1.5 \times 10^{-13} \times (T_e/300)^{-0.42}$	[98, 108]
480	$H_2^+ + e \rightarrow H + H$	$1.6 \times 10^{-14} \times (T_e/300)^{-0.43}$	[98, 109]
Ion-ion recombination			
481	$(CH_3)_2Si^+ + (CH_3)_3Si^- \rightarrow (CH_3)_3Si + (CH_3)_2Si$	9.5×10^{-14}	[56]
482	$(CH_3)_3SiH^+ + (CH_3)_3Si^- \rightarrow (CH_3)_3Si + (CH_3)_3SiH$	8.9×10^{-14}	[56]
483	$(CH_3)_2SiCH_2^+ + (CH_3)_3Si^- \rightarrow (CH_3)_3Si + (CH_3)_2SiCH_2$	9.0×10^{-14}	[56]

Table 2 (continued)

Index	Reaction	Rate coefficient	References
484	$(CH_3)_2SiH^+ + (CH_3)_3Si^- \rightarrow (CH_3)_3Si + (CH_3)_2SiH$	9.5×10^{-14}	[56]
485	$(CH_3)Si^+ + (CH_3)_3Si^- \rightarrow (CH_3)_3Si + (CH_3)Si$	1.0×10^{-13}	[56]
486	$CH_3^+ + (CH_3)_3Si^- \rightarrow (CH_3)_3Si + CH_3$	1.5×10^{-13}	[56]
487	$CH_4^+ + (CH_3)_3Si^- \rightarrow (CH_3)_3Si + CH_4$	1.5×10^{-13}	[56]
488	$CH_2^+ + (CH_3)_3Si^- \rightarrow (CH_3)_3Si + CH_2$	1.6×10^{-13}	[56]
489	$CH^+ + (CH_3)_3Si^- \rightarrow (CH_3)_3Si + CH$	1.6×10^{-13}	[56]
490	$C^+ + (CH_3)_3Si^- \rightarrow (CH_3)_3Si + C$	1.7×10^{-13}	[56]
491	$C_2H_6^+ + (CH_3)_3Si^- \rightarrow (CH_3)_3Si + C_2H_6$	1.2×10^{-13}	[56]
492	$C_2H_5^+ + (CH_3)_3Si^- \rightarrow (CH_3)_3Si + C_2H_5$	1.2×10^{-13}	[56]
493	$C_2H_4^+ + (CH_3)_3Si^- \rightarrow (CH_3)_3Si + C_2H_4$	1.2×10^{-13}	[56]
494	$C_2H_3^+ + (CH_3)_3Si^- \rightarrow (CH_3)_3Si + C_2H_3$	1.2×10^{-13}	[56]
495	$C_2H_2^+ + (CH_3)_3Si^- \rightarrow (CH_3)_3Si + C_2H_2$	1.2×10^{-13}	[56]
496	$H_2^+ + (CH_3)_3Si^- \rightarrow (CH_3)_3Si + H_2$	3.9×10^{-13}	[56]
497	$H^+ + (CH_3)_3Si^- \rightarrow (CH_3)_3Si + H$	5.4×10^{-13}	[56]
498	$Ar^+ + H^- \rightarrow H + Ar[hl]$	6.0×10^{-13}	[56]
499	$Ar_2^+ + H^- \rightarrow H + Ar[2p'] + Ar[1p_0]$	6.0×10^{-13}	[56]
500	$(CH_3)_3Si^+ + H^- \rightarrow H + (CH_3)_3Si$	6.0×10^{-13}	[56]
501	$(CH_3)_2Si^+ + H^- \rightarrow H + (CH_3)_2Si$	6.0×10^{-13}	[56]
502	$CH_3^+ + H^- \rightarrow H + CH_3$	6.2×10^{-13}	[56]
503	$H^+ + H^- \rightarrow 2H$	4.0×10^{-13}	[110]
504	$Ar^+ + CH_2^- \rightarrow CH_2 + Ar[hl]$	2.0×10^{-13}	[56]
505	$Ar_2^+ + CH_2^- \rightarrow CH_2 + Ar[2p'] + Ar[1p_0]$	1.8×10^{-13}	[56]
506	$(CH_3)_3Si^+ + CH_2^- \rightarrow CH_2 + (CH_3)_3Si$	1.8×10^{-13}	[56]
507	$(CH_3)_2Si^+ + CH_2^- \rightarrow CH_2 + (CH_3)_2Si$	1.9×10^{-13}	[56]

Table 2 (continued)

Index	Reaction	Rate coefficient	References
508	$CH_3^+ + CH_2^- \rightarrow CH_2 + CH_3$	2.4×10^{-13}	[56]
Neutral-neutral reactions			
509	$(CH_3)_4Si + (CH_3)_2Si\,(+M) \rightarrow (CH_3)_3SiSi(CH_3)_3\,(+M)$	5.0×10^{-20}	[111]
510	$(CH_3)_3Si + (CH_3)_3Si\,(+M) \rightarrow (CH_3)_3SiSi(CH_3)_3\,(+M)$	2.3×10^{-17}	[112–114]
511	$(CH_3)_3Si + (CH_3)_3Si \rightarrow (CH_3)_2SiCH_2 + (CH_3)_3SiH$	2.0×10^{-18}	[112–114]
512	$(CH_3)_3Si + CH_3\,(+M) \rightarrow (CH_3)_4Si\,(+M)$	1.1×10^{-16}	[115, 116]
513	$(CH_3)_3Si + CH_3 \rightarrow (CH_3)_2SiCH_2 + CH_4$	2.5×10^{-17}	[115, 116]
514	$(CH_3)_3Si + (CH_3)_2SiCH_2\,(+M) \rightarrow (CH_3)_3SiCH_2Si(CH_3)_2\,(+M)$	3.3×10^{-18}	[117]
515	$(CH_3)_3Si + (CH_3)_2SiCH_2\,(+M) \rightarrow (CH_3)_3SiSi(CH_3)_2CH_2\,(+M)$	4.8×10^{-17}	[117]
516	$(CH_3)_3Si + (CH_3)_3SiSi(CH_3)_2CH_2\,(+M) \rightarrow (CH_3)_3SiSi(CH_3)_2CH_2Si(CH_3)_3\,(+M)$	3.0×10^{-17}	[114]
517	$(CH_3)_3Si + (CH_3)_3SiSi(CH_3)_2CH_2 \rightarrow (CH_3)_3SiSi(CH_3)_3 + (CH_3)_2SiCH_2$	2.1×10^{-18}	[114]
518	$(CH_3)_3Si + (CH_3)_3SiCH_2Si(CH_3)_2\,(+M) \rightarrow (CH_3)_3SiSi(CH_3)_2CH_2Si(CH_3)_3\,(+M)$	3.0×10^{-17}	[114]
519	$(CH_3)_3Si + (CH_3)_3SiSi(CH_3)_2\,(+M) \rightarrow (CH_3)_3SiSi(CH_3)_2Si(CH_3)_3\,(+M)$	3.5×10^{-17}	[118]
520	$(CH_3)_3Si + (CH_3)_3SiCH_2\,(+M) \rightarrow (CH_3)_3SiCH_2Si(CH_3)_3\,(+M)$	5.0×10^{-17}	[117]
521	$(CH_3)_3Si + (CH_3)_2SiC_2H_5\,(+M) \rightarrow (CH_3)_3SiSi(CH_3)_2C_2H_5\,(+M)$	3.3×10^{-17}	[117]
522	$(CH_3)_3Si + (CH_3)_2SiH\,(+M) \rightarrow (CH_3)_3SiSiH(CH_3)_2\,(+M)$	6.0×10^{-17}	[118]
523	$(CH_3)_3Si + H\,(+M) \rightarrow (CH_3)_3SiH\,(+M)$	2.0×10^{-16}	[119]
524	$(CH_3)_2Si + (CH_3)_3SiH\,(+M) \rightarrow (CH_3)_3SiSiH(CH_3)_2\,(+M)$	3.5×10^{-18}	[120]
525	$(CH_3)_2Si + (CH_3)_2SiH_2\,(+M) \rightarrow (CH_3)_2HSiSiH(CH_3)_2\,(+M)$	4.9×10^{-18}	[120]
526	$(CH_3)_2Si + (CH_3)_3SiSiH(CH_3)_2\,(+M) \rightarrow (CH_3)_3SiSi(CH_3)_2SiH(CH_3)_2\,(+M)$	4.2×10^{-17}	[111]
527	$(CH_3)_2Si + C_2H_4\,(+M) \rightarrow (CH_3)_2Si\langle \begin{matrix} CH_2 \\ \vert \\ CH_2 \end{matrix}\,(+M)$	2.2×10^{-17}	[121]
528	$(CH_3)_2Si + C_2H_2\,(+M) \rightarrow (CH_3)_2Si\langle \begin{matrix} CH \\ \Vert \\ CH \end{matrix}\,(+M)$	4.6×10^{-17}	[121]

Table 2 (continued)

Index	Reaction	Rate coefficient	References
529	$(CH_3)_2SiCH_2 + (CH_3)_2SiCH_2\,(+M) \rightarrow (CH_3)_2Si\langle \begin{matrix} CH_2 \\ CH_2 \end{matrix} \rangle Si(CH_3)_2\,(+M)$	3.3×10^{-17}	[122]
530	$(CH_3)_2SiCH_2 + CH_3\,(+M) \rightarrow (CH_3)_3SiCH_2\,(+M)$	9.5×10^{-18}	[117]
531	$(CH_3)_2SiCH_2 + CH_3\,(+M) \rightarrow (CH_3)_2SiC_2H_5\,(+M)$	4.8×10^{-18}	[117]
532	$(CH_3)_2SiH + (CH_3)_2SiH \rightarrow (CH_3)_2Si + (CH_3)_2SiH_2$	2.0×10^{-17}	[118, 123]
533	$(CH_3)_2SiH + (CH_3)_2SiH\,(+M) \rightarrow (CH_3)_2HSiSiH(CH_3)_2\,(+M)$	1.0×10^{-17}	[118, 123]
534	$(CH_3)_2SiH + (CH_3)_3SiSi(CH_3)_2\,(+M) \rightarrow (CH_3)_3SiSi(CH_3)_2SiH(CH_3)_2\,(+M)$	1.75×10^{-17}	[118]
535	$(CH_3)_2SiH + (CH_3)_3SiSi(CH_3)_2 \rightarrow (CH_3)_2Si + (CH_3)_3SiSiH(CH_3)_2$	1.75×10^{-17}	[118]
536	$(CH_3)_3SiSiH(CH_3)_2 + H \rightarrow (CH_3)_3SiSi(CH_3)_2 + H_2$	9.2×10^{-19}	[124]
537	$(CH_3)_3SiSiH(CH_3)_2 + H \rightarrow (CH_3)_3Si + (CH_3)_2SiH_2$	8.0×10^{-20}	[124]
538	$(CH_3)_3SiSiH(CH_3)_2 + H \rightarrow (CH_3)_2SiH + (CH_3)_3SiH$	7.1×10^{-20}	[124]
539	$(CH_3)_3SiCH_2Si(CH_3)_2 + CH_3\,(+M) \rightarrow (CH_3)_3SiCH_2Si(CH_3)_3\,(+M)$	4.0×10^{-17}	[117]
540	$(CH_3)_3SiSi(CH_3)_2CH_2 + CH_3\,(+M) \rightarrow (CH_3)_3SiSi(CH_3)_2C_2H_5\,(+M)$	3.0×10^{-17}	[117]
541	$(CH_3)_3SiCH_2 + CH_3\,(+M) \rightarrow (CH_3)_3SiC_2H_5\,(+M)$	4.0×10^{-17}	[117]
542	$(CH_3)_3SiSi(CH_3)_2 + CH_3\,(+M) \rightarrow (CH_3)_3SiSi(CH_3)_3\,(+M)$	3.5×10^{-17}	Analogous to $(CH_3)_3Si$
543	$(CH_3)_2SiC_2H_5 + CH_3\,(+M) \rightarrow (CH_3)_3SiC_2H_5\,(+M)$	4.0×10^{-17}	[117]
544	$Si + C_2H_6\,(+M) \rightarrow (CH_3)_2Si\,(+M)$	3.5×10^{-16}	Analogous to C_2H_4
545	$Si + C_2H_4\,(+M) \rightarrow H_3SiC_2H\,(+M)$	3.5×10^{-16}	[125]
546	$CH_3 + CH_3\,(+Ar) \rightarrow C_2H_6\,(+Ar)$	6.0×10^{-17}	[126, 127]
547	$CH_3 + CH_2 \rightarrow C_2H_4 + H$	2.1×10^{-16}	[128]
548	$CH_3 + CH \rightarrow C_2H_3 + H$	2.0×10^{-16}	[129]
549	$CH_3 + C_2H_5\,(+Ar) \rightarrow C_3H_8\,(+Ar)$	5.6×10^{-17}	[126, 127]
550	$CH_3 + C_2H_5 \rightarrow CH_4 + C_2H_4$	2.0×10^{-18}	[126]
551	$CH_3 + H\,(+Ar) \rightarrow CH_4\,(+Ar)$	3.5×10^{-16}	[126, 127]

Table 2 (continued)

Index	Reaction	Rate coefficient	References
552	$CH_4 + C_2H \rightarrow C_2H_2 + CH_3$	2.3×10^{-18}	[130]
553	$CH_4 + C_2 \rightarrow C_2H + CH_3$	1.7×10^{-17}	[131]
554	$CH_4 + CH \rightarrow C_2H_4 + H$	9.0×10^{-17}	[132]
555	$C_2H_6 + C_2H \rightarrow C_2H_2 + C_2H_5$	3.5×10^{-17}	[133]
556	$C_2H_6 + C_2 \rightarrow C_2H + C_2H_5$	1.6×10^{-16}	[134]
557	$C_2H_6 + CH \rightarrow C_2H_4 + CH_3$	1.3×10^{-16}	[129]
558	$C_2H_6 + CH \rightarrow C_3H_6 + H$	3.0×10^{-17}	[129]
559	$C_2H_5 + C_2H_5\,(+M) \rightarrow C_4H_{10}\,(+M)$	1.9×10^{-17}	[126]
560	$C_2H_5 + C_2H_5 \rightarrow C_2H_6 + C_2H_4$	2.4×10^{-18}	[126]
561	$C_2H_5 + C_2H_3\,(+M) \rightarrow C_4H_8\,(+M)$	2.5×10^{-17}	[135]
562	$C_2H_5 + C_2H_3 \rightarrow 2C_2H_4$	8.0×10^{-19}	[135]
563	$C_2H_5 + C_2H_3 \rightarrow C_2H_6 + C_2H_2$	8.0×10^{-19}	[135]
564	$C_2H_5 + CH_2 \rightarrow CH_3 + C_2H_4$	3.0×10^{-17}	[135]
565	$C_2H_5 + H \rightarrow 2CH_3$	6.0×10^{-17}	[126]
566	$C_2H_4 + C_2H \rightarrow C_2H_2 + C_2H_3$	1.2×10^{-16}	[133]
567	$C_2H_4 + C_2 \rightarrow 2C_2H_2$	3.3×10^{-16}	[134]
568	$C_2H_4 + H\,(+M) \rightarrow C_2H_5\,(+M)$	1.1×10^{-18}	[126, 127]
569	$C_2H_3 + C_2H_3\,(+M) \rightarrow C_4H_6\,(+M)$	1.6×10^{-17}	[135]
570	$C_2H_3 + C_2H_3 \rightarrow C_2H_4 + C_2H_2$	1.6×10^{-18}	[135]
571	$C_2H_3 + CH_2 \rightarrow CH_3 + C_2H_2$	3.0×10^{-17}	[135]
572	$C_2H_3 + H \rightarrow C_2H_2 + H_2$	2.0×10^{-17}	[126]
573	$C_2H + CH_2 \rightarrow CH + C_2H_2$	3.0×10^{-17}	[135]
574	$C_2H + H\,(+M) \rightarrow C_2H_2\,(+M)$	3.0×10^{-16}	[135]
575	$C_2 + H_2 \rightarrow C_2H + H$	1.5×10^{-18}	[136]

Table 2 (continued)

Index	Reaction	Rate coefficient	References
576	$CH_2 + CH_2 \rightarrow C_2H_2 + 2H$	4.7×10^{-17}	[126, 127]
577	$CH_2 + CH_2 \rightarrow C_2H_2 + H_2$	5.3×10^{-18}	[126, 127]
578	$CH_2 + H \rightarrow CH + H_2$	1.4×10^{-16}	[137]
579	$CH + CH\,(+M) \rightarrow C_2H_2\,(+M)$	2.0×10^{-16}	[138]
580	$CH + H_2\,(+M) \rightarrow CH_3\,(+M)$	2.0×10^{-16}	[139]
581	$CH + H \rightarrow C + H_2$	1.0×10^{-16}	[140]
582	$C + H_2\,(+M) \rightarrow CH_2\,(+M)$	7.0×10^{-18}	[141]
583	$C + C\,(+M) \rightarrow C_2\,(+M)$	2.2×10^{-17}	[141]
584	$H + H + Ar \rightarrow H_2 + Ar$	6.0×10^{-42}	[126, 127]

The rate coefficients for two-body and three-body collisions are given in m^3/s and m^6/s, respectively. Rate coefficients $f(u_e)$ are obtained from the solution of the electron Boltzmann equation as a function of the mean electron energy u_e using the cross section data of the reference given. $T_e = 2u_e/(3k_B)$ is the electron temperature in K, and $T_g = 300$ K. Ar^* denotes $Ar[1s_{5..2}]$, Ar[2p], Ar[2p′], and Ar[hl]. Ar_2^* abbreviates $Ar_2[^3\Sigma_u^+, v = 0]$, $Ar_2[^1\Sigma_u^+, v = 0]$, $Ar_2[^3\Sigma_u^+, v \gg 0]$, and $Ar_2[^1\Sigma_u^+, v \gg 0]$

Table 3 Masses M, enthalpies of formation $\Delta H^0_{f,298}$, electron affinities EA, ionization potentials IP, and polarizabilities α_p of neutral species involved in the extended TMS kinetics

Species	Name	M[Da]	$\Delta H^0_{f,298}$[eV]	EA[eV]	IP[eV]	α_p[Å^3]
$(CH_3)_3SiSi(CH_3)_2CH_2Si(CH_3)_3$	Pentamethyl[(trimethylsilyl)methyl]disilane†	218.562				26.11 [50]
$(CH_3)_3SiSi(CH_3)_2Si(CH_3)_3$	Octamethyltrisilane†	204.533	− 4.88 [142]		7.53 [143]	24.27 [50]
$(CH_3)_3SiSi(CH_3)_2SiH(CH_3)_2$	1,1,1,2,2,3,3Heptamethyltrisilane†	190.508				22.42 [50]
$(CH_3)_3SiCH_2Si(CH_3)_3$	Bis(trimethylsilyl)methane†	160.405			9.5 [144]	19.50 [50]
$(CH_3)_3SiSi(CH_3)_2C_2H_5$	Ethylpentamethyldisilane†	160.405			≤ 9.7 [145]	19.50 [50]
$(CH_3)_3SiSi(CH_3)_3$	Hexamethyldisilane	146.378	− 3.76 [142]		8.27 [146]	17.65 [50]
$(CH_3)_3SiCH_2Si(CH_3)_2$	Dimethyl[(trimethylsilyl)methyl]silyl	145.087	− 2.22 [147]			17.28 [50]
$(CH_3)_3SiSi(CH_3)_2CH_2$	[Dimethyl(trimethylsilyl)silyl]methyl	145.087	− 1.67 [147]			17.53 [50]
$(CH_3)_2Si\langle \begin{matrix} CH_2 \\ CH_2 \end{matrix} \rangle Si(CH_3)_2$	1,1,3,3-Tetramethyl-1,3-disilacyclobutane	144.362	− 2.34 [148]		8.56 [149]	16.92 [50]
$(CH_3)_3SiSiH(CH_3)_2$	Pentamethyldisilane	132.352	− 2.86 [150]		≤ 10.2 [151]	15.81 [50]
$(CH_3)_3SiSi(CH_3)_2$	Pentamethyldisilan-1-yl	131.345				15.44 [50]
$(CH_3)_2HSiSiH(CH_3)_2$	1,1,2,2-Tetramethyldisilane†	118.325	− 1.51 [151]		≤ 10.1 [151]	13.96 [50]
$(CH_3)Si\langle \begin{matrix} CH_2 \\ CH_2 \end{matrix} \rangle Si(CH_3)$	1,3-Dimethyl-1,3-disilabicyclo[1.1.0]butane†	114.294				12.51 [50]
$(CH_3)_3SiC_2H_5$	Ethyltrimethylsilane†	102.250	− 3.34 [152]		9.70 [152]	12.89 [50]
$(CH_3)_4Si$	Tetramethylsilane	88.224	− 2.97 [153]		9.80 [154]	11.04 [50]
$(CH_3)_3SiCH_2$	(Trimethylsilyl)methyl	87.217	− 0.30 [155]	0.95 [156]	8.37 [157]	10.92 [50]
$(CH_3)_2SiC_2H_5$	Ethyldimethylsilyl	87.217	0.17[a]		6.80 [158]	10.67 [50]
$(CH_3)_2Si\langle \begin{matrix} CH_2 \\ \vert \\ CH_2 \end{matrix}$	1,1-Dimethylsilirane†	86.209				10.30 [50]
$(CH_3)_2Si\langle \begin{matrix} CH \\ \Vert \\ CH \end{matrix}$	1,1-Dimethylsilirene†	84.193				10.07 [50]
$(CH_3)_3SiH$	Trimethylsilane	74.197	− 1.69 [159]		9.90 [151]	9.19 [50]
$(CH_3)_3Si$	Trimethylsilyl	73.189	− 0.51 [146]	0.97 [61]	7.10 [160]	8.83 [50]

Table 3 (continued)

Species	Name	M[Da]	$\Delta H^0_{f,298}$[eV]	EA[eV]	IP[eV]	α_p[Å^3]
$(CH_3)_2SiCH_2$	Dimethylmethylenesilane	72.181	0.37 [122]		7.71 [161]	8.71 [50]
$(CH_3)_2SiH_2$	Dimethylsilane	60.170	− 0.98 [159]		10.30 [151]	7.35 [50]
$(CH_3)_2SiH$	Dimethylsilyl	59.163	0.93 [162]	1.07 [163]	6.66 [164]	6.98 [50]
$(CH_3)_2Si$	Dimethylsilylene	58.155	0.68 [165]		9.30[b]	6.62[c]
H_3SiC_2H	Ethynylsilane†	56.139	2.23 [166]		10.10 [166]	6.25 [50]
$(CH_3)SiH_2$	Methylsilyl	45.136	1.44 [162]	1.19 [61]	7.39 [164]	5.14 [50]
$(CH_3)SiH$	Methylsilylene	44.128	1.90 [167]		8.77[d]	5.02[e]
$(CH_3)Si$	Methylsilanylidyne	43.120	3.18 [166]	0.85 [168]	7.04 [166]	4.42 [50]
Si	Silicon	28.086	4.66 [169]	1.39 [170]	8.15 [15]	5.38 [15]
C_4H_{10}	n-Butane†	58.122	− 1.30 [171]		10.55 [172]	8.14 [50]
C_4H_8	1-Butene†	56.106	− 0.0065 [173]		9.55 [174]	7.91 [50]
C_4H_6	1,3-Butadiene†	54.090	1.13 [173]		9.07 [175]	7.69 [50]
C_3H_8	Propane†	44.096	− 1.08 [171]		10.94 [176]	6.29 [50]
C_3H_6	Propene†	42.080	0.21 [177]		9.73 [178]	6.07 [50]
C_2H_6	Ethane	30.069	− 0.87 [179]		11.52 [180]	4.44 [50]
C_2H_5	Ethyl	29.061	1.25 [181]	− 0.28 [182]	8.38 [172]	4.33 [50]
C_2H_4	Ethylene	28.053	0.54 [179]		10.51 [15]	4.23 [50]
C_2H_3	Vinyl	27.045	3.10 [183]	0.67 [184]	8.25 [185]	3.78 [50]
C_2H_2	Acetylene	26.037	2.36 [179]		10.40 [15]	3.33 [50]
C_2H	Ethynyl	25.029	4.94 [153]	2.97 [184]	11.61 [186]	3.38 [50]
C_2	Diatomic carbon	24.022	8.68 [153]	3.27 [187]	11.41 [188]	3.45 [50]
CH_4	Methane	16.043	− 0.77 [179]		12.61 [189]	2.58 [55]
CH_3	Methyl	15.035	1.51 [181]	0.08 [190]	9.84 [181]	2.50 [50]
CH_2	Methylene	14.027	4.00 [153]	0.65 [191]	10.40 [15]	2.04 [50]
CH	Methylidyne	13.019	6.16 [153]	1.26 [192]	10.64 [193]	2.11 [50]

Table 3 (continued)

Species	Name	M[Da]	$\Delta H^0_{f,298}$[eV]	EA[eV]	IP[eV]	α_p[Å^3]
C	Carbon	12.011	7.43 [153]	1.26 [170]	11.26 [15]	1.73 [50]
H_2	Hydrogen	2.016	0.0 [169]		15.43 [15]	0.804 [15]
H	Hydrogen atom	1.008	2.26 [169]	0.75 [15]	13.60 [15]	0.667 [15]

[†]Species which are only generated but do not have a collisional loss process

[a]Determined by using enthalpy of formation [152] and ionization potential [158] of the ethyldimethylsilyl ion

[b]Determined by using enthalpy of formation for dimethylsilylene [165] and its ion [151]

[c]Estimated using polarizabilities of dimethylsilyl, dimethylsilane, tetramethylsilane, trimethylsilyl, and methylsilanylidyne given in [50]

[d]Determined by using enthalpy of formation for methylsilylene [167] and its ion [166]

[e]Estimated using polarizabilities of methylsilane, methylsilyl, and methylsilanylidyne given in [50]

Table 4 Nominal masses M/Z and background gas density times mobilities $N\mu_{io}$ of ions considered in the extended TMS kinetics

	Name	M/Z	$N\mu_{io}[10^{21}(\text{V m s})^{-1}]$
Positive ions			
$(CH_3)_2Si\langle \begin{matrix} CH_2 \\ CH_2 \end{matrix} \rangle Si^+CH_3$	1,1,3-trimethyl-1,3-disilacyclobutane-1-yl cation	129	5.3
Ar_2H^+	Argon hydride cation	81	5.6
$(CH_3)_3SiH^+$	Trimethylsilane cation	74	5.7
$(CH_3)_3Si^+$	Trimethylsilyl cation	73	5.7
$(CH_3)_2SiCH_2^+$	Dimethylmethylenesilane cation	72	5.7
$(CH_3)_2SiH^+$	Dimethylsilyl cation	59	5.9
$(CH_3)_2Si^+$	Dimethylsilylene cation	58	6.0
$(CH_3)SiH_2^+$	Methylsilyl cation	45	6.3
$(CH_3)Si^+$	Methylsilanylidyne cation	43	6.4
ArH^+	Argonium	41	6.4
$C_2H_6^+$	Ethane cation	30	7.0
$C_2H_5^+$	Ethyl cation	29	7.1
$C_2H_4^+$	Ethylene cation	28	7.1
$C_2H_3^+$	Vinyl cation	27	7.2
$C_2H_2^+$	Acetylene cation	26	7.3
CH_4^+	Methane cation	16	8.6
CH_3^+	Methyl cation	15	8.8
CH_2^+	Methylene cation	14	9.0
CH^+	Methylidyne cation	13	9.3
C^+	Carbon cation	12	9.5
H_2^+	Molecular hydrogen cation	2	20.9
H^+	Hydrogen cation	1	29.2
Negative ions			
$(CH_3)_3Si^-$	Trimethylsilyl anion	− 73	5.7
CH_2^-	Methylene anion	− 14	9.0
H^-	Hydrogen anion	− 1	29.2

Furthermore, transport coefficients of ions and neutrals are required for the modeling studies. The product of ion mobility times background gas density was determined by use of the polarization mobility [64] obtained from the Langevin theory for all ions. The resulting values are summarized in Table 4. The corresponding diffusion coefficients of the ions were calculated using Einstein's relation [36].

To calculated the diffusion coefficients of the various neutral species in Ar at room temperature, two approaches were applied. The first one is the theory of Chapman and Enskog [194], which requires knowledge about the Lennard-Jones (6-12) potential parameters σ and ϵ/k_B. These parameters are known from the literature for TMS, Si and a number of hydrocarbons as well as atomic and molecular hydrogen and carbon. Furthermore, the empirical relations given in the monograph by Bird et al. [194] were used to determine the Lennard-Jones parameters from the liquid data of the molar volume and boiling point, which are also available in the literature for several stable organosilicon molecules. The

resulting values of diffusion coefficient times background gas density were applied in the numerical modeling studies. They are listed in Table 5.

The second approach to calculate binary-gas phase diffusion coefficients is the diffusion-volume method introduced by Fuller, Schettler and Giddings [195]. This method was used for all other neutral species, where the diffusion volumes for Ar, H, and C were taken from [196] and that for Si was estimated as 27.0 cm^3. This value was found to yield good agreement with results of the Chapman-Enskog theory for most of the silicon- and hydrogen-containing species listed in [44]. The resulting values of diffusion coefficient times background gas density are compiled in Table 5. Notice that the agreement between the values obtained by both the methods is also generally very well for all silicon-containing species included in that table.

Results and Discussion

Model calculations were carried out for Ar-TMS mixtures at atmospheric pressure and a gas temperature of 300 K, with a TMS fraction x between 0 and 200 ppm and an argon amount of $(1 - x)$, in accordance with related experimental studies. The modeling studies comprise an analysis of the ignition voltage of DBDs in Ar-TMS mixtures as well as a characterization of the temporal discharge behavior of such DBDs operating under conditions typical of film-deposition experiments. Therefore, the coupled set of partial differential equations illustrated in Fig. 2 was solved numerically by means of a finite difference method according to Becker et al. [34, 41]. In particular, an adaptive time stepping and a non-equidistant spatial grid using generally 500 intervals with logarithmically refined mesh towards the boundaries were employed for the model calculations reported in "Analysis of the Ignition Voltage" section.

Analysis of the Ignition Voltage

Numerical studies of the ignition voltage U_i were performed for the experimental setup shown in Fig. 1a. They were supplemented by an experimental determination of U_i. For this an HV generator (G2000, Redline Technologies, Baesweiler, Germany) was used to power the discharge with the sinusoidal voltage (1) at $f = 86.2$ kHz, which corresponds to a period duration of $T = 11.6$ µs. The electrical circuit used for measurements of the applied voltage $U_a(t)$ and U_i as well as of the current or transferred charge (see "Temporal Behavior of DBDs in Ar-TMS Mixtures" section) is illustrated in Fig. 3. $U_a(t)$ was measured by means of an HV probe (PHV 4002-3, dataTec, Reutlingen, Germany) connected to an oscilloscope (MDO3052, Tektronix, Beaverton, OR, USA). In order to determine U_i, the amplitude $U_{a,0}$ of the applied voltage was increased step by step for a specific Ar-TMS mixture until the discharge was ignited and covered the entire electrode area, i.e., $U_i = U_{a,0}$. The purity of argon gas (obtained from Linde AG, Germany) was ≥ 99.9999% and that of TMS (from Sigma-Aldrich Chemie GmbH, Germany) was ≥ 99%. The gas flow rate F was 6 slm in the experiments.

Figure 4 shows modeling results of U_i obtained for different sets of rate coefficient k_{M,Ar^*} and Penning ionization fraction α_{Pl} for reactions (2) and (3) of TMS with excited argon atoms in comparison with experimental values. The measured ignition voltage decreases monotonically from about 3.0 kV in pure argon to 1.25 kV at $x = 200$ ppm, where the initially rapid drop becomes smaller above about $x = 50$ ppm. A quite similar

Table 5 Lennard-Jones parameters, and background gas density times binary diffusion coefficients *ND* in argon at 300 K obtained by Chapman-Enskog theory [194] (index CE) and the method of Fuller, Schettler and Giddings [195, 196] (index FSG) using a diffusion volume for Si of 27.0 cm^3

Species	σ[Å]	ϵ/k_B[K]	$ND_{CE}[m^{-1}s^{-1}]$	$ND_{FSG}[m^{-1}s^{-1}]$
$(CH_3)_3SiSi(CH_3)_2CH_2Si(CH_3)_3$				1.1×10^{20}
$(CH_3)_3SiSi(CH_3)_2Si(CH_3)_3$	7.196† [198]	508.2† [198]	1.1×10^{20}	1.1×10^{20}
$(CH_3)_3SiSi(CH_3)_2SiH(CH_3)_2$				1.2×10^{20}
$(CH_3)_3SiCH_2Si(CH_3)_3$	6.692† [198]	468.3† [198]	1.3×10^{20}	1.3×10^{20}
$(CH_3)_3SiSi(CH_3)_2C_2H_5$	6.692† [198]	472.4† [198]	1.3×10^{20}	1.3×10^{20}
$(CH_3)_3SiSi(CH_3)_3$	6.548† [15]	444.7† [15]	1.3×10^{20}	1.4×10^{20}
$(CH_3)_3SiCH_2Si(CH_3)_2$				1.4×10^{20}
$(CH_3)_3SiSi(CH_3)_2CH_2$				1.4×10^{20}
$(CH_3)_2Si\langle \begin{smallmatrix} CH_2 \\ CH_2 \end{smallmatrix} \rangle Si(CH_3)_2$	6.306† [198]	452.7† [198]	1.4×10^{20}	1.4×10^{20}
$(CH_3)_3SiSiH(CH_3)_2$	6.340† [198]	428.7† [198]	1.4×10^{20}	1.5×10^{20}
$(CH_3)_3SiSi(CH_3)_2$				1.5×10^{20}
$(CH_3)_2HSiSiH(CH_3)_2$	6.127† [198]	413.6† [198]	1.5×10^{20}	1.6×10^{20}
$(CH_3)Si\langle \begin{smallmatrix} CH_2 \\ CH_2 \end{smallmatrix} \rangle Si(CH_3)$				1.6×10^{20}
$(CH_3)_3SiC_2H_5$	5.889† [198]	381.6† [198]	1.6×10^{20}	1.7×10^{20}
$(CH_3)_4Si$	8.137 [199]	223.1 [199]	1.2×10^{20}	1.8×10^{20}
$(CH_3)_3SiCH_2$				1.8×10^{20}
$(CH_3)_2SiC_2H_5$				1.8×10^{20}
$(CH_3)_2Si\langle \begin{smallmatrix} CH_2 \\ \vert \\ CH_2 \end{smallmatrix}$				1.9×10^{20}
$(CH_3)_2Si\langle \begin{smallmatrix} CH \\ \Vert \\ CH \end{smallmatrix}$				1.9×10^{20}
$(CH_3)_3SiH$	5.447† [200]	321.8† [200]	2.0×10^{20}	2.0×10^{20}
$(CH_3)_3Si$				2.1×10^{20}
$(CH_3)_2SiCH_2$				2.1×10^{20}
$(CH_3)_2SiH_2$	5.563† [200]	236.0† [200]	2.1×10^{20}	2.3×10^{20}
$(CH_3)_2SiH$				2.4×10^{20}
$(CH_3)_2Si$				2.4×10^{20}
H_3SiC_2H				2.5×10^{20}
$(CH_3)SiH_2$				2.9×10^{20}
$(CH_3)SiH$				2.9×10^{20}
$(CH_3)Si$				3.0×10^{20}
Si	2.005 [201]	18640 [201]	3.0×10^{20}	4.3×10^{20}
C_4H_{10}	4.687 [202]	531.4 [202]	2.2×10^{20}	2.2×10^{20}
C_4H_8	4.994† [198]	306.9† [198]	2.3×10^{20}	2.3×10^{20}
C_4H_6	4.903† [198]	309.1† [198]	2.4×10^{20}	2.4×10^{20}
C_3H_8	4.724† [203]	265.7† [203]	2.7×10^{20}	2.7×10^{20}
C_3H_6	4.579† [203]	259.3† [203]	2.8×10^{20}	2.8×10^{20}
C_2H_6	4.443 [202]	215.7 [202]	3.3×10^{20}	3.4×10^{20}
C_2H_5				3.5×10^{20}

Table 5 (continued)

Species	σ[Å]	ϵ/k_B[K]	ND_{CE}[$m^{-1}s^{-1}$]	ND_{FSG}[$m^{-1}s^{-1}$]
C_2H_4	4.163 [202]	224.7 [202]	3.6×10^{20}	3.6×10^{20}
C_2H_3				3.8×10^{20}
C_2H_2	4.033 [202]	231.8 [202]	3.8×10^{20}	3.9×10^{20}
C_2H				4.0×10^{20}
C_2	3.913 [202]	78.8 [202]	4.8×10^{20}	4.2×10^{20}
CH_4	3.882 [197]	136.5 [197]	5.1×10^{20}	5.2×10^{20}
CH_3	3.905 [204]	88.1 [204]	5.6×10^{20}	5.6×10^{20}
CH_2	3.905 [204]	59.4 [204]	6.0×10^{20}	5.9×10^{20}
CH	3.370 [202]	68.6 [202]	7.0×10^{20}	6.3×10^{20}
C	3.385 [202]	30.6 [202]	7.9×10^{20}	6.8×10^{20}
H_2	2.827 [202]	59.7 [202]	1.9×10^{21}	2.2×10^{21}
H	2.708 [202]	37.0 [202]	2.9×10^{21}	3.6×10^{21}

The Lennard-Jones parameters for argon are $\sigma = 3.418$Å and $\epsilon/k_B = 124.0$ K [197]. †: estimated from empirical relations given on page 22 of [194] using molar volume and boiling point given in the reference

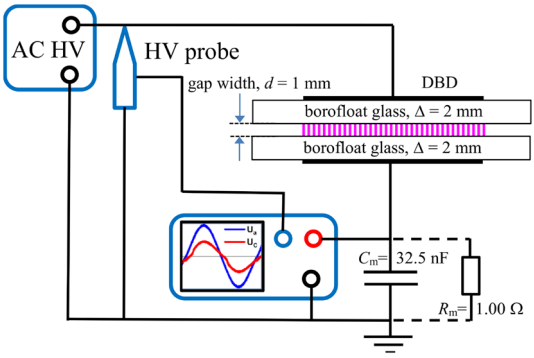

Fig. 3 Electrical circuit used for voltage and current measurements

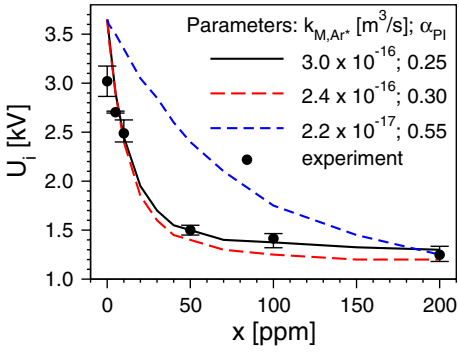

Fig. 4 Ignition voltages obtained by measurements and by modeling using different parameter sets of k_{M,Ar^*} and α_{PI} in dependence on the TMS fraction x

behavior of the ignition voltage for mixtures of Ar and HMDSO was reported for the same DBD configuration in [35]. There, the monotonic decrease resulted in $U_i = 1.0\,\mathrm{kV}$ at $x = 200\,\mathrm{ppm}$ and it could be well described by modeling results, when employing the measured rate coefficient of $5.0 \times 10^{-16}\,\mathrm{m^3/s}$ [58] for Ar*-HMDSO reactions and a corresponding Penning ionization fraction of 30% in the reaction kinetics model.

The decrease of U_i with increasing TMS admixture obtained from the experiments is also found by the modeling studies for all sets of k_{M,Ar^*} and α_{Pl}, which assume a certain amount of Penning ionization processes. In particular, best agreement between measured and calculated results is obtained, when 25 % of the reactions of TMS with Ar* are supposed to lead to the generation of electrons due to Penning ionization at a total rate coefficient $k_{M,Ar^*} = 3.0 \times 10^{-16}\,\mathrm{m^3/s}$. The assumption of $\alpha_{Pl} = 0.3$ and $k_{M,Ar^*} = 2.4 \times 10^{-16}\,\mathrm{m^3/s}$ in the model calculations also leads to quite good agreement with the measured U_i, but the variation with x is not reproduced similarly well. Both these rate coefficients are more than a magnitude larger than that determined experimentally by Jauberteau et al. [57] in the afterglow of a microwave discharge by means of absorption spectroscopy measurements on Ar[$1s_5$]. The measured total rate coefficient in that paper ranged from 6.0×10^{-18} to $2.2 \times 10^{-17}\,\mathrm{m^3/s}$. When using the latter value in the model calculations, a Penning ionization fraction for Ar*-TMS reactions of 55% has to be applied to achieve agreement with the measured ignition voltage at $x = 200\,\mathrm{ppm}$. However, the decreasing behavior of the measured U_i with increasing x cannot be reproduced that way. Finally, it should be noted that the modeling results obtained by use of the reduced reaction kinetics scheme (Table 1) are identical to those obtained when employing the extended plasma-chemistry model (Tables 1 and 2).

In order to analyze the ionization budget at the ignition voltage for different TMS fractions x in more detail, the space- and period-averaged ionization rates of the different electron production processes were determined from the modeling results using the recommended total rate coefficient $k_{M,Ar^*} = 3.0 \times 10^{-16}\,\mathrm{m^3/s}$ and Penning ionization fraction $\alpha_{Pl} = 0.25$. Figure 5 illustrates the corresponding relative contributions of different reaction channels to the total electron production in dependence on x. In pure argon, electrons are produced to about 60% due to electron impact ionization of argon atoms in their ground state and to about 40% due to chemo-ionization processes in collisions of two excited argon atoms. The contributions of electron impact ionization of excited argon atoms and molecules, respectively, to the total electron production are less than 1% in pure argon and much smaller when adding TMS. Therefore, they are not displayed in the figure.

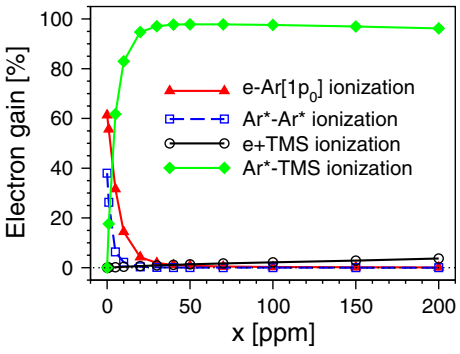

Fig. 5 Impact of the TMS fraction x on the electron production channels for applied voltage amplitudes $U_i(x)$

When adding small amounts of TMS to argon, the situation changes drastically. Since the ionization energy of TMS (9.80 ± 0.03 eV) and the appearance energy of the trimethylsilyl cation (10.03 ± 0.04 eV) [154] are smaller than the threshold energies for the excitation of argon atoms (≥ 11.55 eV) [34, 205], the admixture of TMS is accompanied in particular by the electron production due to Penning ionization according to (2), i.e. reactions 10–16 in Table 1. This collision process becomes the predominant contribution to the electron production already for $x \geq 5$ ppm. Here, more than 99.9% of these electrons are produced by reactions of metastable ($1s_5$ and $1s_3$) and resonance ($1s_4$ and $1s_2$) atoms. At the same time, the contribution of the electron-Ar[$1p_0$] ionization and of the chemo-ionization due to Ar^*-Ar^* collisions decreases and becomes less than 1% for $x > 40$ ppm and $x > 10$ ppm, respectively. The contribution of electron impact ionization of TMS increases monotonically with rising TMS fraction, but it contributes to the total electron production only to about 4% for $x = 200$ ppm. Furthermore, detachment processes of the negative trimethylsilyl ion $(CH_3)_3Si^-$ due to collisions with electrons and excited argon species (reactions 6 and 29-39 in Table 1) are found to be insignificant. Moreover, contributions of further species involved in the extended reaction kinetics scheme related to TMS (cf. Table 2) are also negligible because their particle number densities are too small during the ignition phase.

Temporal Behavior of DBDs in Ar-TMS Mixtures

The analysis of the temporal behavior of DBDs operating under conditions typical of deposition experiments was carried out for Ar-TMS mixtures with an initial TMS fraction x up to 200 ppm. Model calculations were done for an applied voltage amplitude $U_{a,0} = 4$ kV and a frequency $f = 86.2$ kHz employing the extended plasma-chemistry model of TMS (Tables 1, 2). Here, a non-equidistant spatial grid using 250 intervals with logarithmically refined mesh towards the boundaries was employed. The temporal evolution of the discharge behavior was followed for the residence time $t_r = V/F$ of the gas mixture in the plasma zone with a volume of $V = A \times d = 0.8\,cm^3$ including the effect of TMS depletion, where $t_r = 8$ ms, i.e., about 690 periods, for the gas flow rate $F = 6$ slm in related experiments.

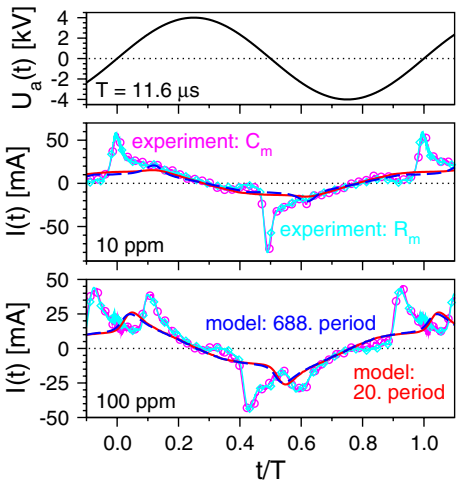

Fig. 6 Calculated temporal behavior of the discharge current at $U_{a,0} = 4$ kV and $f = 86.2$ kHz for the initial TMS fractions $x = 10$ and 100 ppm in comparison with measured data

Figure 6 displays the applied voltage $U_a(t)$ and the calculated temporal evolution of the discharge current

$$I(t) = \frac{A}{d}\int_0^d \left[\varepsilon_0 \frac{\partial}{\partial t} E(z,t) + e_0 \sum_j Z_j \Gamma_j(z,t)\right] \mathrm{d}z \tag{4}$$

for Ar-TMS mixtures with an initial fraction x of TMS of 10 and 100 ppm, respectively, using the recommended total rate coefficient $k_{M,Ar^*} = 3.0 \times 10^{-16}\,\mathrm{m^3/s}$ and Penning ionization fraction $\alpha_{PI} = 0.25$ for the numerical modeling. Here, modeling results of the 20. and 688. period are shown starting at the instants $t_0 = 0.23$ and 7.98 ms for $t/T = 0$ in this figure. These results are compared with measured data of the periodic behavior of the discharge current. Here, the oscilloscope (MDO3052 from Tektronix, Beaverton, OR, USA) was used to monitor the voltage drop at the precision resistor $R_M = 1.00\Omega$ or the measuring capacitor $C_M = 32.5\,\mathrm{nF}$ (see Fig. 3), from which $I(t)$ or the transferred charge $Q(t)$ and, thus again the current $I(t) = \mathrm{d}Q(t)/(\mathrm{d}t)$, were obtained. A recent discussion related to measurements of the DBD actuator power consumption using the shunt resistor method and the monitor capacitor method, respectively, is given in [206].

There are quite different aspects which become obvious from Fig. 6. First of all, it can be seen that the measured and calculated discharge currents are of the same order of magnitude, where the results of both measurements using R_M and C_M agree fairly well. At the same time, the comparison of the measured current with the modeling results makes it clear that the measured temporal course of $I(t)$ cannot completely be reproduced by the model calculations. On the one hand, these differences can be attributed to the relatively large effect of electrode edges and the resulting fringing electric fields, which occur at the small-scale electrode configuration investigated with a length of only 1 cm in gas flow direction. For example, an experimental value of 6.6 pF was obtained for the cell capacitance [33], a factor of 1.74 larger than that calculated using the equation for an ideal parallel-plate capacitor (3.79 pF). Here, a spatially two-dimensional model is required. However, such model is currently not available and applicable because of the tremendous computational times to be expected, since the current time-dependent, spatially one-dimensional model calculations including the complete Ar-TMS reaction kinetics already required about 4 months on a single CPU at 3.2 GHz to reach $t_r = 8$ ms. In addition, the reason for the two discharge peaks per half-period found in the experiments at $x = 100$ ppm with similar intensity in the positive half-period, but different intensity in the negative half-period is unclear so far.

On the other hand, the spatially one-dimensional modeling results provide helpful insights into the electrical characteristics as well as the reaction products and processes of DBDs in Ar-TMS mixtures. When comparing the modeling results of the 20. and 688. period for initially $x = 100$ ppm TMS, it becomes clear that the calculated discharge current remains almost the same during the flow of the plasma across the discharge area, which lasts $t_r = 8$ ms (Fig. 6). Here, the single discharge peak per half-period results to a large extent from Penning ionization due to collisions of excited argon atoms with TMS molecules. These Penning ionization processes are also the main source of electrons at the beginning of the calculated temporal evolution for $x = 10$ ppm and lead to a comparatively small current peak (20. period), similar to the discharge current behavior in Ar-HMDSO mixtures discussed in [35]. At the end of the calculations around $t_r = 8$ ms (688. period) the single peak of the discharge current per half-period is more pronounced and the temporal evolution of $I(t)$ shows great similarities to the behavior in

pure Ar (cf. Figure 7 in [35]). This change of the calculated discharge current from the initial condition at $t = 0$ to the end of the gas flow through the discharge area at $t_r = 8$ ms is a direct consequence of the change of the composition of the discharge plasma and the corresponding change of dominant processes leading to the generation of electrons.

In order to illustrate the temporal change of the composition of the gas and of relevant species of the plasma during the residence time, Figs. 7, 8, 9 and 10 display results for various particle number densities obtained by model calculations for Ar-TMS mixtures with initially $x = 10$ and 100 ppm TMS. Here, spatially averaged densities are shown. Furthermore, the spatially averaged mean energy of the electrons is represented in Fig. 9. Notice that the temporal evolution of period-averaged species densities and electron mean energy are exhibited to avoid a too noisy representation resulting from the temporal change during each period of duration $T = 11.6$ µs.

At initially $x = 10$ ppm a drastic decrease of TMS is found during the temporal discharge development by a factor of 350 until $t_r = 8$ ms, i.e., TMS is virtually completely consumed at t_r (Fig. 7a). It leads mainly to the generation of methane (CH_4) and trimethylsilane ($(CH_3)_3SiH$) during the first about 2 ms and predominantly to hydrogen molecules (H_2) in the later phase. Further stable molecules that are effectively generated and to be mentioned are ethylene (C_2H_4), ethane (C_2H_6), acetylene (C_2H_2), and hexamethyldisilane ($(CH_3)_3SiSi(CH_3)_3$). Their production is a consequence of neutral-neutral collision processes involving radical species (Fig. 8a). Here, the primary radicals trimethylsilyl ($(CH_3)_3Si$) and methyl (CH_3) are predominant at the beginning, while the hydrogen atom becomes leading for times greater than about 2 ms. In addition to several hydrocarbon radicals, further silicon-containing radicals, namely dimethylsilyl ($(CH_3)_2SiH$), dimethylsilylene ($(CH_3)_2Si$), [dimethyl(trimethylsilyl)silyl]methyl ($(CH_3)_3SiSi(CH_3)_2CH_2$), methylsilanylidyne ($(CH_3)Si$), and methylsilyl ($(CH_3)SiH_2$), are also formed during the temporal evolution and also still have a remarkable number density in some cases at $t_r = 8$ ms, such as $(CH_3)_2SiH$.

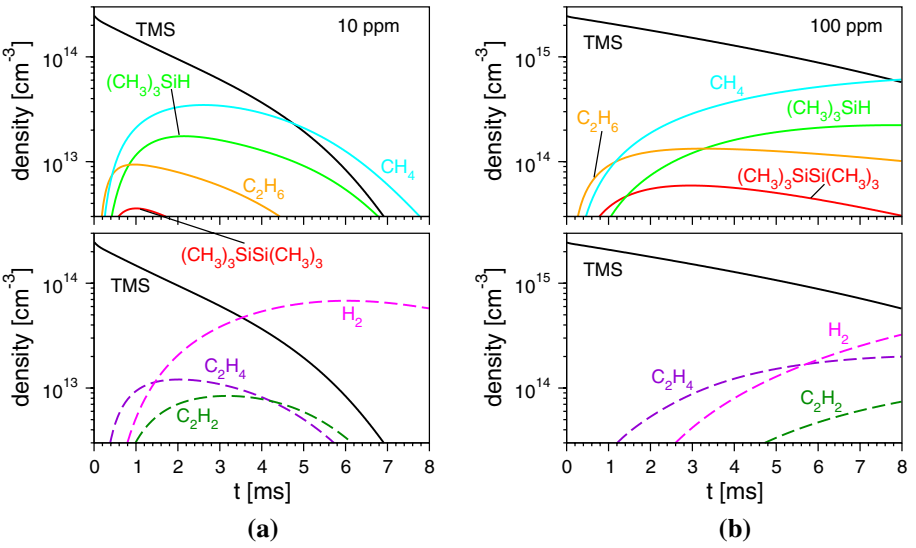

Fig. 7 Temporal evolution of particle densities of stable molecules for $U_{a,0} = 4$ kV, $f = 86.2$ kHz, and the initial TMS fraction, **a** $x = 10$ ppm and **b** $x = 100$ ppm

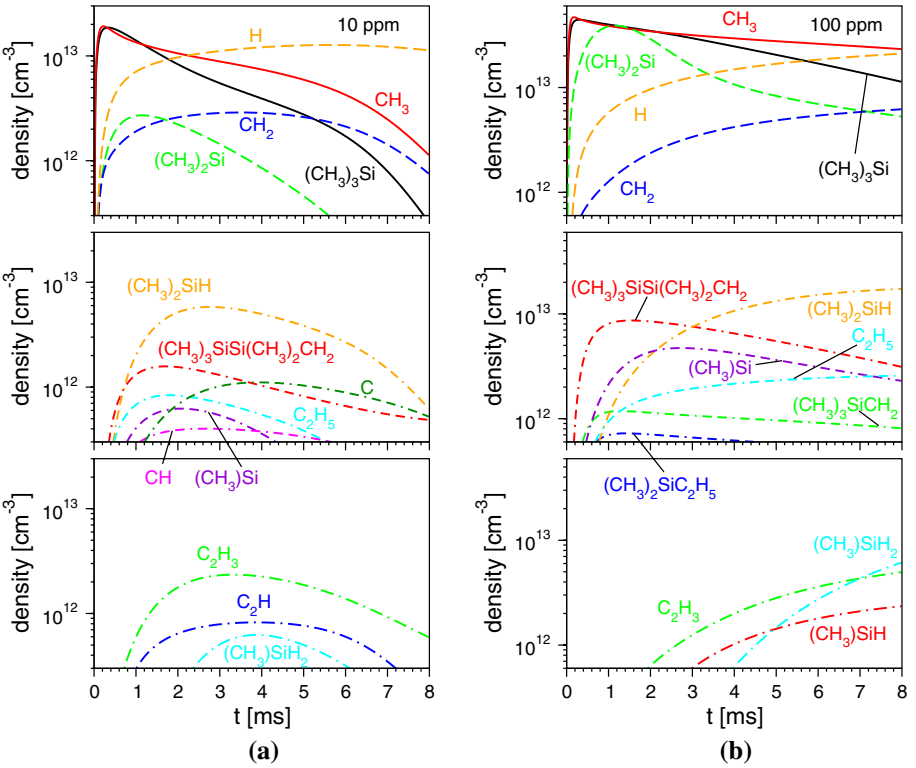

Fig. 8 Temporal evolution of particle densities as in Fig. 7 but for radical species

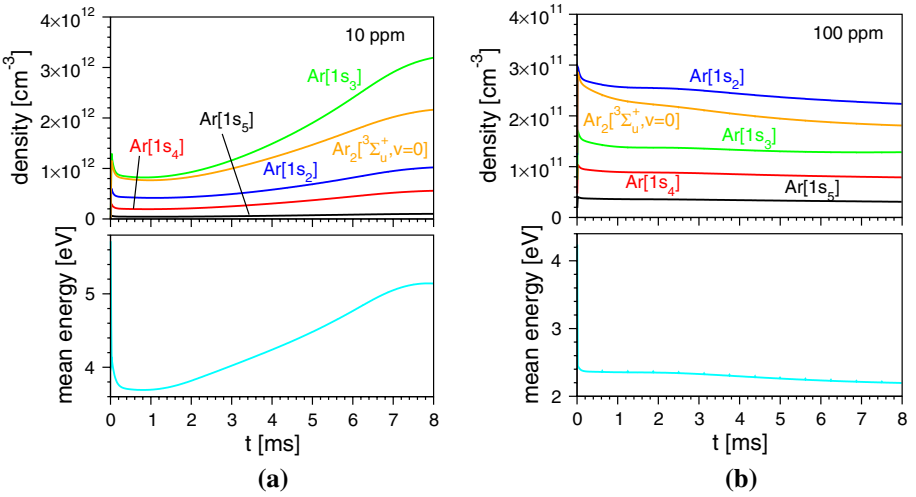

Fig. 9 Temporal evolution as in Fig. 7 but for particle densities of excited argon species and the mean electron energy

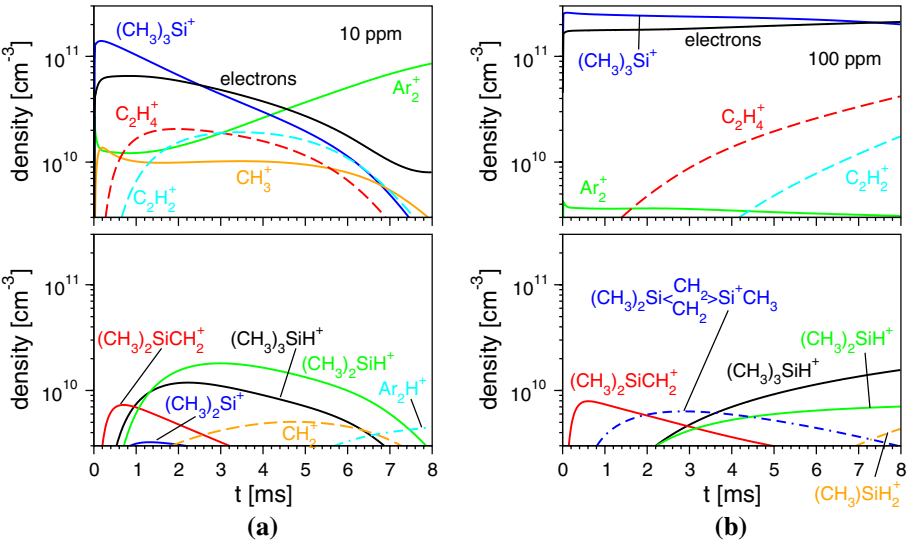

Fig. 10 Temporal evolution of particle densities as in Fig. 7 but for charge carriers

The decrease of TMS is primarily caused by collisional quenching in collisions with excited argon species (Fig. 9a), predominantly by metastable Ar[1s$_3$] atoms and the excimer $Ar_2[^3\Sigma_u^+, v = 0]$, followed by the resonance Ar[1s$_2$] and Ar[1s$_4$] atoms. Here, 25% of the collision processes of excited argon atoms with TMS each lead to the generation of an electron, a trimethylsilyl cation, a methyl radical, and Ar[1p$_0$] due to Penning ionization (Fig. 10a). Measurements of particle number densities of metastable and resonance argon atoms could help to confirm the predictions about their absolute value and relative contribution predicted by the model.

When keeping in mind that the background gas density of ground state argon atoms is 2.45×10^{19} cm^{-3} and that H_2, CH_4, and C_2H_6 are not able to generate electrons due to Penning ionization processes with excited argon atoms, it is immediately clear that the discharge current behavior has to change in the course of time from an initially Penning ionization dominated one to a behavior predominantly determined by electron-impact ionization of Ar[1p$_0$] atoms at initially $x = 10$ ppm (cf. Fig. 6). This transition is continuously supported by the increase of the mean electron energy leading to an increase of the number densities of excited argon species (Fig. 9a). At the same time the electron density decreases and molecular argon ions become the leading charge carrier (Fig. 10a). Negative ions play a negligible role for the discharge behavior, where the most prominent one, $(CH_3)_3Si^-$, has a number density of $\leq 10^8$ cm^{-3} during the entire temporal evolution. Here, it has to be noted that all silicon-containing and hydrocarbon cations are generated to a certain extent due to Penning ionization processes, while the Ar_2H^+ ion results from charge-transfer reactions of Ar_2^+ with H_2 molecules. Note further that quasi-neutrality is limited to the main discharge phase and exists only in the plasma bulk region. Due to the applied sinusoidal voltage, electrons drift fast to the dielectric walls where they are partly lost. Hence electron-ion recombination plays a minor role for the discharge behavior. Thus, the sum of space- and period-averaged number densities of all cations exceeds that of electrons plus all anions as it becomes obvious from Fig. 10.

When looking at the modeling results for the initial TMS fraction $x = 100$ ppm, the almost same behavior of the discharge current at the 20. and 688. period (cf. Fig. 6) indicates that a quite different temporal evolution of the various particle number densities and the mean electron energy can be expected. Their development during the residence time $t_r = 8$ ms is shown in part b of Figs. 7, 8, 9 and 10.

Again, TMS decreases mainly due to collisions with excited argon species, but the reduction of TMS is by about 75% only (Fig. 7b). Further modeling results show that, for instance, TMS reduces by 90% at initially $x = 50$ ppm, while 50% of the monomer remain after $t_r = 8$ ms at $x = 200$ ppm. This finding agrees well with the analysis provided by [30], where the consumption of TMS in an atmospheric-pressure Ar-TMS microplasma was found to be more effective at low TMS concentrations compared with their consumptions at high concentrations. A similar trend of monomer depletion in a large-area atmospheric-pressure DBD in Ar-HMDSO mixtures was recently discussed in [37]. This decrease of the percentage monomer consumption during the residence time of the plasma in the discharge with increasing monomer fraction is a direct consequence of the finite number of excited argon species available to dissociate and/or ionize the monomer via energy transfer.

The main stable molecules generated in the Ar-TMS DBD for initially $x = 100$ ppm are the same as for $x = 10$ ppm (Fig. 7). However, the composition of the plasma is different. Here, methane becomes the predominant species at $t_r = 8$ ms, except for the background ground gas argon with a number density of 2.45×10^{19} cm^{-3}. After TMS, molecular hydrogen, trimethylsilane, and ethylene follow. Since the latter two species as well as acetylene and hexamethyldisilane are also able to generated electrons due to collision processes with excited argon atoms, about 40% of the species relevant to the TMS kinetics contribute to Penning ionization at $t_r = 8$ ms. Furthermore it should be mentioned that further silicon-containing stable molecules are generated during the temporal evolution, which reach particle number densities above 3×10^{13} cm^{-3}. These species are 1,1-dimethylsilirane, 1,1-dimethylsilirene, 1,1,1,2,2,3,3-heptamethyltrisilane, ethylpentamethyldisilane, and pentamethyl[(trimethylsilyl)methyl]disilane (cf. Table 3) and their space- and period-averaged particle number densities at $t_r = 8$ ms amount to 2.2×10^{14} cm^{-3}, 8.6×10^{13} cm^{-3}, 6.3×10^{13} cm^{-3}, 5.3×10^{13} cm^{-3}, and 4.5×10^{13} cm^{-3}, respectively. However, they are only generated in the framework of the present reaction kinetics model and do not have any collisional loss process so that these values appear to be upper limits.

Most of the radical species already found at $x = 10$ ppm are also generated at the initial TMS fraction of 100 ppm (Fig. 8b). However, the share of these species changes, where in particular the amount and particle number density of silicon-containing radicals increases. In addition to trimethylsilyl, dimethylsilylene, dimethylsilyl, and [dimethyl(trimethylsilyl) silyl]methyl are effectively formed during the temporal evolution. Furthermore, methylsilanylidyne and methylsilyl as well as (trimethylsilyl)methyl and methylsilylene are formed (cf. Table 3), where the latter two species are not present at initially $x = 10$ ppm. Moreover, methyl is the predominant hydrocarbon radical, and hydrogen atoms are again generated to a considerable extent (Fig. 8b).

When comparing the excited argon species at $x = 10$ and 100 ppm (Fig. 9), it becomes obvious that the more effective quenching due to collisions with TMS at the larger TMS admixture leads to a decrease of the absolute number densities of these species by about one order of magnitude. For initially $x = 100$ ppm, the resonance Ar[$1s_2$] atom is largest, followed by the excimer $Ar_2[^3\Sigma_u^+, v = 0]$ and the sequence of the further Ar[$1s_j$] levels with $j = 3 - 5$ decreasing with increasing j, i.e., decreasing energy level (Fig. 9b). At the same time, the number density of all these particles shows a monotonous reduction, which comes along with the slight decrease of the mean electron energy.

Despite the slow decline of their mean energy, the space- and period-averaged number density of electrons rises steadily, mainly due to Penning ionization processes of excited argon atoms, where the trimethylsilyl cation is the main ionic species during the entire temporal evolution (Fig. 10b). Except for ethylene and acetylene ions, the number densities of all other ions remain smaller by more than one order of magnitude than that of $(CH_3)_3Si^+$. In addition to the dimethylmethylenesilane, trimethylsilane and dimethylsilyl cations, the methylsilyl ion and especially the 1,1,3-trimethyl-1,3-disilacyclobutane-1-yl ion with a mass to charge ratio of 129 are predicted by the model calculations (cf. Table 4). The latter originates from collision processes of 1,1,3,3-tetramethyl-1,3-disilacyclobutane (Table 3) mainly with excited argon atoms leading to Penning ionization. Notice that several of the positive ions were also reported in the studies of an atmospheric-pressure microplasma with Ar-TMS containing 280, 1600, and 3500 ppm, respectively, of TMS [30]. These are the ions with the nominal mass M/Z 15, 26, 28, 45, 58, 59, 73, and 129 (cf. Table 4). However, the silicon-containing trimethylsilane ion ($M/Z = 74$) and dimethylmethylenesilane ion ($M/Z = 72$) (Fig. 10) were not found in that study. Again, the particle number densities of all negative ions remain small in the Ar-TMS DBD with initially $x = 100$ ppm, namely $\leq 10^9$ cm^{-3}, 2×10^8 cm^{-3}, and 3×10^7 cm^{-3} for $(CH_3)_3Si^-$, H^-, and CH_2^-, respectively.

The results for the number densities of radicals and charge carriers obtained by numerical modeling (Figs. 8 and 10) suggest that radicals are the predominant species for the film formation in plasma polymerization at atmospheric pressure [24]. Corresponding argumentations are also given when discussing the deposition of thin films using atmospheric-pressure DBDs with admixture of the monomers HMDSO or tetraethoxysilane (TEOS) [13, 33, 35, 207–210]. However, not the particle number density is the key for the film formation, but the flux of particles towards the surface. In order to get an impression of main particle fluxes at the dielectric surface at $z_0 = d$ in front of the grounded electrode (cf. Fig. 1b), Fig. 11 shows the temporal evolution of the particle fluxes of main radicals and charge carriers. Here, period-averaged fluxes $\langle \Gamma_j(d,t) \rangle_T$ are displayed for the initial TMS fractions

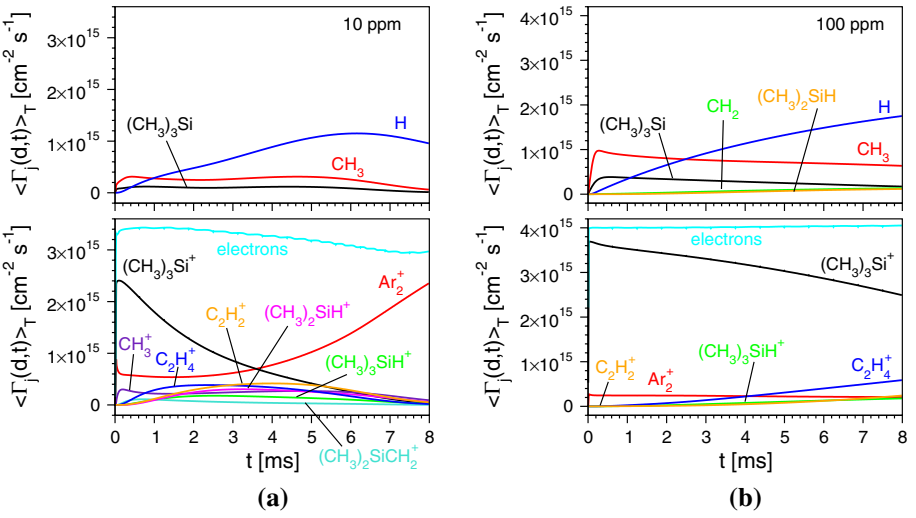

Fig. 11 Temporal evolution of particle flux of radicals and charge carriers at the boundary $z_0 = d$ for $U_{a,0} = 4$ kV, $f = 86.2$ kHz, and the initial TMS fraction, **a** $x = 10$ ppm and **b** $x = 100$ ppm

$x = 10$ and 100 ppm. Apart from the electrons, the flux of trimethylsilyl cations is predominant at $x = 100$ ppm and at beginning of the temporal evolution at $x = 10$ ppm as well. Moreover, the $(CH_3)_3Si^+$ flux is always larger than the flux of the most prominant silicon-containing radial $(CH_3)_3Si$, where larger TMS fractions result in an increasing dominance of the flux of positive trimethylsilyl ions. This finding means that ions and not radicals are mainly responsible for the film formation in atmospheric-pressure plasma polymerization using DBDs with Ar-TMS mixtures.

Conclusion

The impact on the discharge characteristics of atmospheric-pressure argon DBDs caused by admixing up to 200 ppm TMS has been analyzed by means of a time-dependent, spatially one-dimensional fluid-Poisson model. It involves, in particular, an established reaction kinetics scheme for argon and an extended plasma-chemistry model including about 60 species and 580 reactions related to TMS.

Based on good agreement of modeling results with corresponding measurements of the ignition voltage, it is found that the rate coefficient for collision processes of TMS with excited Ar[$1s_5$] atoms [57] and the fraction leading to Penning ionization [57, 59] are underestimated so far. Best agreement between measured and calculated data is obtained for a total collision rate coefficient of TMS with excited argon atoms of $3 \times 10^{-16}\,m^3/s$, assuming that 25% of that reaction lead to the generation of electrons due to Penning ionization.

The numerical modeling studies clearly demonstrate the significant impact of small amounts of TMS on the temporal behavior of Ar-TMS DBDs operating under conditions typical of deposition experiments. It is found that TMS is largely depleted at low admixtures, while a growing amount of this monomer remains available for film formation with increasing TMS admixture. Trimethylsilane and hexamethyldisilane are found to be the major silicon-containing stable molecules generated during the residence time of the plasma in the DBD, and trimethylsilyl, dimethylsilylene, dimethylsilane, and [dimethyl(trimethylsilyl)silyl]methyl are the most prominent radicals containing Si.

The analysis clearly indicates as well that trimethylsilyl cations can be considered to be mainly responsible for the film formation. This result is strongly supported by first experimental results related to a single-filament DBD in Ar-HMDSO mixtures, where pentamethyldisiloxanyl cations, generated from HMDSO via Penning ionization due to collisions with excited argon atoms, are found to be the dominant species to form the film [211]. Thus, the present modeling studies raise the serious question, if the current knowledge of the processes leading to the formation of organosilicon films has to be reconsidered or revised. Further combined experimental and modeling studies on that finding can help to clarify the fundamental understanding of main species and reaction pathways for the formation of organosilicon polymer films.

Acknowledgements The work was partly funded by the Deutsche Forschungsgemeinschaft (DFG, German Research Foundation)—project numbers 5451831, 213099213, and 213099267. The authors thank J. Philipp very much for his assistance in the electrical measurements.

Funding Open Access funding provided by Projekt DEAL.

Data Availability The datasets related to the comparison between modeling and experimental results shown in Figs. 4 and 6 are available in the research data platform INPTDAT [212]. Further datasets generated and analyzed during the current study are available from the corresponding author on reasonable request.

References

1. Tajima I, Yamamoto M (1987) J Polym Sci A Polym Chem 25(7):1737. https://doi.org/10.1002/pola.1987.080250703
2. Wróbel AM, Czeremuszkin G, Szymanowski H, Kowalski J (1990) Plasma Chem Plasma Process 10(2):277. https://doi.org/10.1007/BF01447131
3. Favia P, Lamendola R, d'Agostino R (1992) Plasma Sources Sci Technol 1(1):59. https://doi.org/10.1088/0963-0252/1/1/007
4. Zhang W, Lelogeais M, Ducarroir M (1992) Jpn J Appl Phys 31(12R):4053. https://doi.org/10.1143/JJAP.31.4053
5. Peter S, Pintaske R, Hecht G, Richter F (1993) Surf Coat Technol 59(1):97. https://doi.org/10.1016/0257-8972(93)90061-R
6. Fonseca JLC, Apperley DC, Badyal JPS (1993) Chem Mater 5(11):1676. https://doi.org/10.1021/cm00035a015
7. Grill A, Patel V (1999) J Appl Phys 85(6):3314. https://doi.org/10.1063/1.369677
8. Han LM, Pan JS, Chen S-M, Balasubramanian N, Shi J, Wong LS, Foo PD (2001) J Electrochem Soc 148(7):F148. https://doi.org/10.1149/1.1375797
9. Yanguas-Gil Á, Barranco Á, Cotrino J, Gröning P, González-Elipe AR (2006) Chem Vap Depos 12(12):728. https://doi.org/10.1002/cvde.200606496
10. Soum-Glaude A, Thomas L, Tomasella E (2006) Surf Coat Technol 200(22):6425. https://doi.org/10.1016/j.surfcoat.2005.11.066
11. Kihel M, Sahli S, Zenasni A, Raynaud P, Segui Y (2014) Vacuum 107:264. https://doi.org/10.1016/j.vacuum.2014.02.022
12. Kurunczi P, Koharian A, Becker K, Martus K (1996) Contrib Plasma Phys 36(6):723. https://doi.org/10.1002/ctpp.2150360608
13. Sonnenfeld A, Tun TM, Zajíčková L, Kozlov KV, Wagner H-E, Behnke JF, Hippler R (2001) Plasmas Polym 6(4):237. https://doi.org/10.1023/A:1014414016164
14. Ipolyi I, Burean E, Hamann T, Cingel M, Matejcik S, Swiderek P (2009) Int J Mass Spectrom 282(3):133. https://doi.org/10.1016/j.ijms.2009.02.020
15. Lide DR (ed) (2009) CRC handbook of chemistry and physics, 90th edn. CRC Press, Boca Raton
16. Rynders SW, Scheeline A, Bohn PW (1991) J Appl Phys 69(5):2951. https://doi.org/10.1063/1.348606
17. Fonseca JLC, Tasker S, Apperley DC, Badyal JPS (1996) Macromolecules 29(5):1705. https://doi.org/10.1021/ma950222v
18. Thomas L, Maillé L, Badie JM, Ducarroir M (2001) Surf Coat Technol 142–144:314. https://doi.org/10.1016/S0257-8972(01)01081-7
19. Soum-Glaude A, Thomas L, Dollet A, Picard C (2007) Plasma Process Polym 4(1):S11. https://doi.org/10.1002/ppap.200730201
20. Soum-Glaude A, Thomas L, Dollet A, Ségur P, Bordage M-C (2007) Diam Relat Mater 16(4):1259. https://doi.org/10.1016/j.diamond.2006.11.003
21. Massines F, Sarra-Bournet C, Fanelli F, Naudé N, Gherardi N (2012) Plasma Process Polym 9(11–12):1041. https://doi.org/10.1002/ppap.201200029
22. Merche D, Vandencasteele N, Reniers F (2012) Thin Solid Films 520(13):4219. https://doi.org/10.1016/j.tsf.2012.01.026

23. Raballand V, Benedikt J, von Keudell A (2008) Appl Phys Lett 92(9):091502. https://doi.org/10.1063/1.2844880
24. Marchand DJ, Dilworth ZR, Stauffer RJ, Hsiao E, Kim J-H, Kang J-G, Kim SH (2013) Surf Coat Technol 234:14. https://doi.org/10.1016/j.surfcoat.2013.03.029
25. Kwong CH, Ng SP, Kan CW, Molina R (2014) Fibers Polym 15(8):1596. https://doi.org/10.1007/s12221-014-1596-7
26. Kan CW, Kwong CH, Ng SP (2015) Appl Surf Sci 346:270. https://doi.org/10.1016/j.apsusc.2015.03.111
27. Kan CW, Kwong CH, Ng SP (2015) Fibers Polym 16(3):702. https://doi.org/10.1007/s12221-015-0702-9
28. Kan C-W, Kwong C-H, Ng S-P (2016) Appl Sci 6(2):59. https://doi.org/10.3390/app6020059
29. Kan CW, Kwong CH, Ng SP (2016) J Text Inst 107(1):91. https://doi.org/10.1080/00405000.2015.1012880
30. Haq AU, Lucke P, Benedikt J, Maguire P, Mariotti D (2020) Plasma Process Polym 17(5):1900243. https://doi.org/10.1002/ppap.201900243
31. Kogelschatz U (2003) Plasma Chem Plasma Process 23(1):1. https://doi.org/10.1023/A:1022470901385
32. Philipp J, Czerny AK, Klages C-P (2016) Plasma Process Polym 13(5):509. https://doi.org/10.1002/ppap.201500136
33. Klages C-P, Czerny AK, Philipp J, Becker MM, Loffhagen D (2017) Plasma Process Polym 14(12):1700081. https://doi.org/10.1002/ppap.201700081
34. Becker MM, Hoder T, Brandenburg R, Loffhagen D (2013) J Phys D Appl Phys 46(35):355203. https://doi.org/10.1088/0022-3727/46/35/355203
35. Loffhagen D, Becker MM, Czerny AK, Philipp J, Klages C-P (2018) Contrib Plasma Phys 58(5):337. https://doi.org/10.1002/ctpp.201700060
36. Fridman A (2008) Plasma chemistry. Cambridge University Press, New York
37. Loffhagen D, Becker MM, Hegemann D, Nisol B, Watson S, Wertheimer MR, Klages C-P (2020) Plasma Process Polym 17(2):1900169. https://doi.org/10.1002/ppap.201900169
38. Höft H, Kettlitz M, Becker MM, Hoder T, Loffhagen D, Brandenburg R, Weltmann K-D (2014) J Phys D Appl Phys 47(46):465206. https://doi.org/10.1088/0022-3727/47/46/465206
39. Ponduri S, Becker MM, Welzel S, van de Sanden MCM, Loffhagen D, Engeln R (2016) J Appl Phys 119(9):093301. https://doi.org/10.1063/1.4941530
40. Becker MM, Loffhagen D (2013) AIP Adv 3:012108. https://doi.org/10.1063/1.4775771
41. Becker MM, Kählert H, Sun A, Bonitz M, Loffhagen D (2017) Plasma Sources Sci Technol 26(4):044001. https://doi.org/10.1088/1361-6595/aa5cce
42. Leyh H, Loffhagen D, Winkler R (1998) Comput Phys Commun 113(1):33. https://doi.org/10.1016/S0010-4655(98)00062-9
43. Vass M, Korolov I, Loffhagen D, Pinhão N, Donkó Z (2017) Plasma Sources Sci Technol 26(6):065007. https://doi.org/10.1088/1361-6595/aa6789
44. Perrin J, Leroy O, Bordage M-C (1996) Contrib Plasma Phys 36(1):3. https://doi.org/10.1002/ctpp.2150360102
45. Bordage M-C (2007) Plasma Sci Technol 9(6):756. https://doi.org/10.1088/1009-0630/9/6/28
46. Ali MA, Kim Y-K, Hwang W, Weinberger NM, Rudd ME (1997) J Chem Phys 106(23):9602. https://doi.org/10.1063/1.473842
47. Peart B, Forrest R, Dolder KT (1979) J Phys B At Mol Phys 12(3):L115. https://doi.org/10.1088/0022-3700/12/3/009
48. Walton DS, Peart B, Dolder KT (1971) J Phys B At Mol Phys 4(10):1343. https://doi.org/10.1088/0022-3700/4/10/019
49. Peart B, Forrest R, Dolder KT (1979) J Phys B At Mol Phys 12(5):847. https://doi.org/10.1088/0022-3700/12/5/028
50. http://www.chemicalize.org (2018)
51. Velazco JE, Kolts JH, Setser DW (1978) J Chem Phys 69(10):4357. https://doi.org/10.1063/1.436447
52. Oka T, Kogoma M, Imamura M, Arai S, Watanabe T (1979) J Chem Phys 70(7):3384. https://doi.org/10.1063/1.437923
53. Carles S, Le Garrec JL, Mitchell JBA (2007) J Chem Phys 127(14):144308. https://doi.org/10.1063/1.2774984
54. Bardsley JN, Biondi MA (1970) Advances in atomic and molecular physics, vol 6. Academic Press, New York

55. Johnston DR, Oudemans GJ, Cole RH (1960) J Chem Phys 33(5):1310. https://doi.org/10.1063/1.1731405
56. Hickman AP (1979) J Chem Phys 70(11):4872. https://doi.org/10.1063/1.437364
57. Jauberteau JL, Jauberteau I, Aubreton J (2000) Chem Phys Lett 327(5):351. https://doi.org/10.1016/S0009-2614(00)00854-X
58. Jauberteau JL, Jauberteau I (2012) J Phys Chem A 116(35):8840. https://doi.org/10.1021/jp304694z
59. Anderson DR, Bierbaum VM, Depuy CH, Grabowski JJ (1983) Int J Mass Spectrom Ion Phys 52(1):65. https://doi.org/10.1016/0020-7381(83)85092-X
60. Creatore M, Barrell Y, Benedikt J, van de Sanden MCM (2006) Plasma Sources Sci Technol 15(3):421. https://doi.org/10.1088/0963-0252/15/3/018
61. Wetzel DM, Salomon KE, Berger S, Brauman JI (1989) J Am Chem Soc 111(11):3835. https://doi.org/10.1021/ja00193a013
62. Thomson JJ (1912) Philos Mag 23(136):449. https://doi.org/10.1080/14786440408637241
63. Rudge MRH (1964) Proc Phys Soc 83(3):419. https://doi.org/10.1088/0370-1328/83/3/309
64. Viehland LA, Mason EA (1995) At Data Nucl Data Tables 60(1):37. https://doi.org/10.1006/adnd.1995.1004
65. Deutsch H, Becker K, Basner R, Schmidt M, Märk TD (1998) J Phys Chem A 102(45):8819. https://doi.org/10.1021/jp9827577
66. Bell KL, Gilbody HB, Hughes JG, Kingston AE, Smith FJ (1983) J Phys Chem Ref Data 12(4):891. https://doi.org/10.1063/1.555700
67. Shah MB, Elliott DS, Gilbody HB (1987) J Phys B At Mol Phys 20(14):3501. https://doi.org/10.1088/0022-3700/20/14/022
68. Freund RS, Wetzel RC, Shul RJ, Hayes TR (1990) Phys Rev A 41:3575. https://doi.org/10.1103/PhysRevA.41.3575
69. Kim Y-K, Stone PM (2007) J Phys B At Mol Opt Phys 40(8):1597. https://doi.org/10.1088/0953-4075/40/8/011
70. Jiao CQ, Garscadden A, Haaland PD (1999) Int J Mass Spectrom 184(1):83. https://doi.org/10.1016/S1387-3806(98)14270-7
71. Hwang W, Kim Y-K, Rudd ME (1996) J Chem Phys 104(8):2956. https://doi.org/10.1063/1.471116
72. Straub HC, Lin D, Lindsay BG, Smith KA, Stebbings RF (1997) J Chem Phys 106(11):4430. https://doi.org/10.1063/1.473468
73. Kim Y-K, Ali MA, Rudd ME (1997) J Res Natl Inst Stand Technol 102(6):693. https://doi.org/10.6028/jres.102.046
74. Chatham H, Hils D, Robertson R, Gallagher A (1984) J Chem Phys 81(4):1770. https://doi.org/10.1063/1.447848
75. Nishimura H, Tawara H (1994) J Phys B At Mol Opt Phys 27(10):2063. https://doi.org/10.1088/0953-4075/27/10/016
76. Song M-Y, Yoon J-S, Cho H, Karwasz GP, Kokoouline V, Nakamura Y, Tennyson J (2017) J Phys Chem Ref Data 46(1):013106. https://doi.org/10.1063/1.4976569
77. Yoon J-S, Song M-Y, Han J-M, Hwang SH, Chang W-S, Lee B, Itikawa Y (2008) J Phys Chem Ref Data 37(2):913. https://doi.org/10.1063/1.2838023
78. Peart B, Walton DS, Dolder KT (1970) J Phys B At Mol Phys 3(10):1346. https://doi.org/10.1088/0022-3700/3/10/012
79. Rawat P, Prabhudesai VS, Rahman MA, Bhargava Ram N, Krishnakumar E (2008) Int J Mass Spectrom 277(1):96. https://doi.org/10.1016/j.ijms.2008.05.015
80. Song M-Y, Yoon J-S, Cho H, Itikawa Y, Karwasz GP, Kokoouline V, Nakamura Y, Tennyson J (2015) J Phys Chem Ref Data 44(2):023101. https://doi.org/10.1063/1.4918630
81. Shishikura Y, Asano K, Nakamura Y (1997) J Phys D Appl Phys 30(11):1610. https://doi.org/10.1088/0022-3727/30/11/010
82. Rutkowsky J, Drost H, Spangenberg H-J (1980) Ann Phys 492(4):259. https://doi.org/10.1002/andp.19804920404
83. May O, Fedor J, Allan M (2009) Phys Rev A 80:012706. https://doi.org/10.1103/PhysRevA.80.012706
84. Ehrhardt AB, Langer WD (1987) Collisional processes of hydrocarbons in hydrogen plasmas. Tech. Rep. PPPL-2477, Plasma Physics Laboratory, Princeton University, Princeton, New Jersey 08544, USA
85. Nakano T, Toyoda H, Sugai H (1991) Jpn J Appl Phys 30(11R):2908. https://doi.org/10.1143/JJAP.30.2908
86. Nakano T, Toyoda H, Sugai H (1991) Jpn J Appl Phys 30(11R):2912. https://doi.org/10.1143/JJAP.30.2912

87. Janev RK, Reiter D (2004) Phys Plasmas 11(2):780. https://doi.org/10.1063/1.1630794
88. Shul RJ, Upschulte BL, Passarella R, Keesee RG, Castleman AW (1987) J Phys Chem 91(10):2556. https://doi.org/10.1021/j100294a022
89. Praxmarer C, Hansel A, Lindinger W, Herman Z (1998) J Chem Phys 109(11):4246. https://doi.org/10.1063/1.477073
90. Tsuji M, Kouno H, Matsumura K, Funatsu T, Nishimura Y, Obase H, Kugishima H, Yoshida K (1993) J Chem Phys 98(3):2011. https://doi.org/10.1063/1.464234
91. Dotan I, Lindinger W (1982) J Chem Phys 76(10):4972. https://doi.org/10.1063/1.442843
92. Adams NG, Bohme DK, Ferguson EE (1970) J Chem Phys 52(10):5101. https://doi.org/10.1063/1.1672748
93. Potzinger P, Lampe FW (1971) J Phys Chem 75(1):13. https://doi.org/10.1021/j100671a002
94. Phelps AV (1992) J Phys Chem Ref Data 21(4):883. https://doi.org/10.1063/1.555917
95. Jones EG, Harrison AG (1970) Int J Mass Spectrom Ion Phys 5(1–2):137. https://doi.org/10.1016/0020-7381(70)87012-7
96. Balamuta J, Golde MF, Ho Y-S (1983) J Chem Phys 79(6):2822. https://doi.org/10.1063/1.446103
97. Thomas RD, Kashperka I, Vigren E, Geppert WD, Hamberg M, Larsson M, af Ugglas M, Zhaunerchyk V, Indriolo N, Yagi K, Hirata S, McCall BJ (2012) Astrophys J 758(1):55. https://doi.org/10.1088/0004-637X/758/1/55
98. Mitchell JBA (1990) Phys Rep 186(5):215. https://doi.org/10.1016/0370-1573(90)90159-Y
99. Mul PM, Mitchell JBA, D'Angelo VS, Defrance P, McGowan JW, Froelich HR (1981) J Phys B At Mol Phys 14(8):1353. https://doi.org/10.1088/0022-3700/14/8/020
100. Bates DR (1986) Astrophys J 306:L45. https://doi.org/10.1086/184702
101. Adams NG, Smith D (1988) Chem Phys Lett 144(1):11. https://doi.org/10.1016/0009-2614(88)87081-7
102. Geppert W, Ehlerding A, Hellberg F, Kalhori S, Thomas RD, Novotny O, Arnold ST, Miller TM, Viggiano AA, Larsson M (2004) Phys Rev Lett 93:153201. https://doi.org/10.1103/PhysRevLett.93.153201
103. Bates DR (1989) Astrophys J 344:531. https://doi.org/10.1086/167823
104. Ehlerding A, Hellberg F, Thomas R, Kalhori S, Viggiano AA, Arnold ST, Larsson M, af Ugglas M (2004) Phys Chem Chem Phys 6:949. https://doi.org/10.1039/B314882C
105. Mul PM, McGowan JW (1980) Astrophys J 237:749. https://doi.org/10.1086/157921
106. Kalhori S, Viggiano AA, Arnold ST, Rosén S, Semaniak J, Derkatch AM, af Ugglas M, Larsson M (2002) Astron Astrophys 391(3):1159. https://doi.org/10.1051/0004-6361:20020882
107. Derkatch AM, Al-Khalili A, Vikor L, Neau A, Shi W, Danared H, af Ugglas M, Larsson M (1999) J Phys B At Mol Opt Phys 32(14):3391. https://doi.org/10.1088/0953-4075/32/14/309
108. Mitchell JBA, McGowan JW (1978) Astrophys J 222:L77. https://doi.org/10.1086/182696
109. Hus H, Yousif F, Noren C, Sen A, Mitchell JBA (1988) Phys Rev Lett 60:1006. https://doi.org/10.1103/PhysRevLett.60.1006
110. Moseley J, Aberth W, Peterson JR (1970) Phys Rev Lett 24:435. https://doi.org/10.1103/PhysRevLett.24.435
111. Baggott JE, Blitz MA, Frey HM, Lightfoot PD, Walsh R (1987) Chem Phys Lett 135(1):39. https://doi.org/10.1016/0009-2614(87)87213-5
112. Shimo N, Nakashima N, Yoshihara K (1986) Chem Phys Lett 125(3):303. https://doi.org/10.1016/0009-2614(86)87070-1
113. Safarik I, Jodhan A, Strausz OP, Bell TN (1987) Chem Phys Lett 142(1):115. https://doi.org/10.1016/0009-2614(87)87262-7
114. Kerst C, Potzinger P, Wagner HG (1995) J Photochem Photobiol A Chem 90(1):19. https://doi.org/10.1016/1010-6030(95)04086-U
115. Niiranen JT, Gutman D (1993) J Phys Chem 97(37):9392. https://doi.org/10.1021/j100139a023
116. Tokach SK, Koob RD (1980) J Phys Chem 84(1):1. https://doi.org/10.1021/j100438a001
117. Ahmed M, Potzinger P, Wagner HG (1995) J Photochem Photobiol A Chem 86(1–3):33. https://doi.org/10.1016/1010-6030(94)03953-R
118. Kerst C, Potzinger P, Wagner HG (1996) Z Naturforsch 51A(1–2):105. https://doi.org/10.1515/zna-1996-1-216
119. Ellul R, Potzinger P, Reimann B (1984) J Phys Chem 88(13):2793. https://doi.org/10.1021/j150657a024
120. Baggott JE, Blitz MA, Frey HM, Walsh R (1990) J Am Chem Soc 112(23):8337. https://doi.org/10.1021/ja00179a018
121. Baggott JE, Blitz MA, Frey HM, Lightfoot PD, Walsh RR (1988) J Chem Soc Faraday Trans 2 84:515. https://doi.org/10.1039/F29888400515

122. Brix T, Arthur NL, Potzinger P (1989) J Phys Chem 93(25):8193. https://doi.org/10.1021/j100362a011
123. Kerst C, Potzinger P, Wagner HG (1996) Z Naturforsch 51A(1–2):102. https://doi.org/10.1515/zna-1996-1-215
124. Fabry L, Potzinger P, Reimann B, Ritter A, Steenbergen HP (1986) Organometallics 5(6):1231. https://doi.org/10.1021/om00137a030
125. Canosa A, Le Picard SD, Gougeon S, Rebrion-Rowe C, Travers D, Rowe BR (2001) J Chem Phys 115(14):6495. https://doi.org/10.1063/1.1396855
126. Baulch DL, Cobos CJ, Cox RA, Frank P, Hayman G, Just T, Kerr JA, Murrells T, Pilling MJ, Troe J, Walker RW, Warnatz J (1994) J Phys Chem Ref Data 23(6):847. https://doi.org/10.1063/1.555953
127. Baulch DL, Cobos CJ, Cox RA, Frank P, Hayman G, Just T, Kerr JA, Murrells T, Pilling MJ, Troe J, Walker RW, Warnatz J (1995) J Phys Chem Ref Data 24(4):1609. https://doi.org/10.1063/1.555975
128. Wang B, Fockenberg C (2001) J Phys Chem A 105(37):8449. https://doi.org/10.1021/jp011350q
129. Galland N, Caralp F, Hannachi Y, Bergeat A, Loison J-C (2003) J Phys Chem A 107(28):5419. https://doi.org/10.1021/jp027465r
130. Opansky BJ, Leone SR (1996) J Phys Chem 100(12):4888. https://doi.org/10.1021/jp9532677
131. Matsugi A, Suma K, Miyoshi A (2010) J Phys Chem A 114(13):4580. https://doi.org/10.1021/jp1012494
132. Blitz MA, Johnson DG, Pesa M, Pilling MJ, Robertson SH, Seakins PW (1997) J Chem Soc Faraday Trans 93:1473. https://doi.org/10.1039/A607617C
133. Opansky BJ, Leone SR (1996) J Phys Chem 100(51):19904. https://doi.org/10.1021/jp9619604
134. Pasternack L, McDonald JR (1979) Chem Phys 43(2):173. https://doi.org/10.1016/0301-0104(79)85185-X
135. Tsang W, Hampson RF (1986) J Phys Chem Ref Data 15(3):1087. https://doi.org/10.1063/1.555759
136. Nakajima M, Matsugi A, Miyoshi A (2009) J Phys Chem A 113(31):8963. https://doi.org/10.1021/jp904165s
137. Zabarnick S, Fleming JW, Lin MC (1986) J Chem Phys 85(8):4373. https://doi.org/10.1063/1.451808
138. Braun W, McNesby JR, Bass AM (1967) J Chem Phys 46(6):2071. https://doi.org/10.1063/1.1841003
139. Fulle D, Hippler H (1997) J Chem Phys 106(21):8691. https://doi.org/10.1063/1.473930
140. Harding LB, Guadagnini R, Schatz GC (1993) J Phys Chem 97(21):5472. https://doi.org/10.1021/j100123a005
141. Martinotti FF, Welch MJ, Wolf AP (1968) Chem Commun (Lond) 115–116. https://doi.org/10.1039/C19680000115
142. Pedley JB, Rylance J (1977) Sussex-N.P.L. Computer analysed thermochemical data: organic and organometallic compounds. University of Sussex, Brighton, England
143. Pitt CG, Bursey MM, Rogerson PF (1970) J Am Chem Soc 92(3):519. https://doi.org/10.1021/ja00706a016
144. Hosomi A, Traylor TG (1975) J Am Chem Soc 97(13):3682. https://doi.org/10.1021/ja00846a020
145. Davidson IMT, Stephenson IL (1967) J Organometal Chem 7(2):P24. https://doi.org/10.1016/S0022-328X(00)91064-7
146. Szepes L, Baer T (1984) J Am Chem Soc 106(2):273. https://doi.org/10.1021/ja00314a002
147. Davidson IMT, Potzinger P, Reimann B (1982) Ber Bunsenges Phys Chem 86(1):13. https://doi.org/10.1002/bbpc.19820860104
148. Genchel' VG, Demidova NV, Nametkin NS, Gusel'nikov LE, Volnina EA, Burdasov EN, Vdovin VM (1976) Russ Chem Bull 25(10):2181. https://doi.org/10.1007/BF02659543
149. Pitt CG, Habercom MS, Bursey MM, Rogerson PF (1968) J Organometal Chem 15(2):359. https://doi.org/10.1016/S0022-328X(00)91314-7
150. Walsh R (1989) Organometallics 8(8):1973. https://doi.org/10.1021/om00110a021
151. Potzinger P, Ritter A, Krause J, Naturforsch Z A (1975) 30:347. https://doi.org/10.1515/zna-1975-0314
152. Hess GG, Lampe FW, Sommer LH (1965) J Am Chem Soc 87(23):5327. https://doi.org/10.1021/ja00951a012
153. Chase MW (1998) Phys J, Chem. Ref. Data Monograph 9, 1. NIST-JANAF Thermochemical Tables, 4th edn. Part I, Al-Co
154. Murphy MK, Beauchamp JL (1977) J Am Chem Soc 99(7):2085. https://doi.org/10.1021/ja00449a013
155. Allendorf MD, Melius CF (1992) J Phys Chem 96(1):428. https://doi.org/10.1021/j100180a080
156. Wetzel DM, Brauman JI (1988) J Am Chem Soc 110(25):8333. https://doi.org/10.1021/ja00233a008
157. Coote ML, Lin CY, Beckwith ALJ, Zavitsas AA (2010) Phys Chem Chem Phys 12:9597. https://doi.org/10.1039/C003880F

158. Davidson IMT, Stephenson IL (1968) J Chem Soc A. 282. https://doi.org/10.1039/J19680000282
159. Doncaster AM, Walsh R (1986) J Chem Soc Faraday Trans 2 82:707. https://doi.org/10.1039/F29868200707
160. Band SJ, Davidson IMT, Lambert CA, Stephenson IL (1967) Chem Commun (Lond) 723. https://doi.org/10.1039/C19670000723
161. Dyke JM, Josland GD, Lewis RA, Morris A (1982) J Phys Chem 86(15):2913. https://doi.org/10.1021/j100212a022
162. Casserly TB, Gleason KK (2005) Plasma Process Polym 2(9):669. https://doi.org/10.1002/ppap.200500054
163. Brinkman EA, Berger S, Brauman JI (1994) J Am Chem Soc 116(18):8304. https://doi.org/10.1021/ja00097a042
164. Chatgilialoglu C (1995) Chem Rev 95(5):1229. https://doi.org/10.1021/cr00037a005
165. Davidson IMT, Matthews JI (1976) J Chem Soc Faraday Trans 1 72:1403. https://doi.org/10.1039/F19767201403
166. Ketvirtis AE, Bohme DK, Hopkinson AC (1995) J Phys Chem 99(43):16121. https://doi.org/10.1021/j100043a063
167. Walsh R (1988) Organometallics 7(1):75. https://doi.org/10.1021/om00091a014
168. Bengali AA, Leopold DG (1992) J Am Chem Soc 114(23):9192. https://doi.org/10.1021/ja00049a064
169. Chase MW (1998) Phys J Chem. Ref. Data Monograph 9, 959. NIST-JANAF Thermochemical Tables, 4th edn. Part II, Cr-Zr
170. Scheer M, Bilodeau RC, Brodie CA, Haugen HK (1998) Phys Rev A 58:2844. https://doi.org/10.1103/PhysRevA.58.2844
171. Pittam DA, Pilcher G (1972) J Chem Soc Faraday Trans 1 68:2224. https://doi.org/10.1039/F19726802224
172. Rosenstock HM, Draxl K, Steiner BW, Herron JT (1977) J Phys Chem Ref Data 6(Suppl. 1):1
173. Prosen EJ, Maron FW, Rossini FD (1951) J Res NBS 46(2):106. https://nvlpubs.nist.gov/nistpubs/jres/46/jresv46n2p106_A1b.pdf
174. van der Meij CE, van Eck J, Niehaus A (1989) Chem Phys 130(1):325. https://doi.org/10.1016/0301-0104(89)87061-2
175. Mallard WG, Miller JH, Smyth KC (1983) J Chem Phys 79(12):5900. https://doi.org/10.1063/1.445770
176. Stockbauer R, Inghram MG (1971) J Chem Phys 54(5):2242. https://doi.org/10.1063/1.1675158
177. Furuyama S, Golden DM, Benson SW (1969) J Chem Thermodyn 1(4):363. https://doi.org/10.1016/0021-9614(69)90066-4
178. Traeger JC (1984) Int J Mass Spectrom Ion Process 58:259. https://doi.org/10.1016/0168-1176(84)80034-8
179. Manion JA (2002) J Phys Chem Ref Data 31(1):123. https://doi.org/10.1063/1.1420703
180. Luo Y-R, Pacey PD (1992) Int J Mass Spectrom Ion Process 112(1):63. https://doi.org/10.1016/0168-1176(92)87032-A
181. Berkowitz J, Ellison GB, Gutman D (1994) J Phys Chem 98(11):2744. https://doi.org/10.1021/j100062a009
182. DePuy CH, Gronert S, Barlow SE, Bierbaum VM, Damrauer R (1989) J Am Chem Soc 111(6):1968. https://doi.org/10.1021/ja00188a003
183. DeFrees DJ, McIver RT, Hehre WJ (1980) J Am Chem Soc 102(10):3334. https://doi.org/10.1021/ja00530a005
184. Ervin KM, Gronert S, Barlow SE, Gilles MK, Harrison AG, Bierbaum VM, DePuy CH, Lineberger WC, Ellison GB (1990) J Am Chem Soc 112(15):5750. https://doi.org/10.1021/ja00171a013
185. Blush JA, Chen P (1992) J Phys Chem 96(11):4138. https://doi.org/10.1021/j100190a004
186. Norwood K, Ng CY (1989) J Chem Phys 91(5):2898. https://doi.org/10.1063/1.456960
187. Arnold DW, Bradforth SE, Kitsopoulos TN, Neumark DM (1991) J Chem Phys 95(12):8753. https://doi.org/10.1063/1.461211
188. Reid CJ, Ballantine JA, Andrews SR, Harris FM (1995) Chem Phys 190(1):113. https://doi.org/10.1016/0301-0104(94)00335-8
189. Berkowitz J, Greene JP, Cho H, Ruscić B (1987) J Chem Phys 86(2):674. https://doi.org/10.1063/1.452268
190. Ellison GB, Engelking PC, Lineberger WC (1978) J Am Chem Soc 100(8):2556. https://doi.org/10.1021/ja00476a054
191. Leopold DG, Murray KK, Miller AES, Lineberger WC (1985) J Chem Phys 83(10):4849. https://doi.org/10.1063/1.449746

192. Goebbert DJ (2012) Chem Phys Lett 551:19. https://doi.org/10.1016/j.cplett.2012.08.065
193. Herzberg G, Johns JWC (1969) Astrophys J 158:399. https://doi.org/10.1086/150202
194. Bird RB, Stewart WE, Lightfoot EN (1960) Transport phenomena. Wiley, New York
195. Fuller EN, Schettler PD, Giddings JC (1966) Ind Eng Chem 58(5):19. https://doi.org/10.1021/ie50677a007
196. Fuller EN, Ensley K, Giddings JC (1969) J Phys Chem 73(11):3679. https://doi.org/10.1021/j100845a020
197. Hirschfelder JO, Bird RB, Spotz EL (1949) Chem Rev 44(1):205. https://doi.org/10.1021/cr60137a012
198. https://www.lookchem.com (2019). CAS Nos. 106-98-9, 106-99-0, 812-15-7, 814-98-2, 1627-98-1, 2117-28-4, 3439-38-1, 3704-44-7, 15063-64-6
199. Marcos DH, Lindley DD, Wilson KS, Kay WB, Hershey HC (1983) J Chem Thermodyn 15(11):1003. https://doi.org/10.1016/0021-9614(83)90024-1
200. Schön H (2015) Handbook of purified gases. Springer, Berlin. https://doi.org/10.1007/978-3-540-32599-4
201. L'vov BV, Nikolaev VG (1987) J Appl Spectrosc 46(1):1. https://doi.org/10.1007/BF00660271
202. Shevla RA (1962) Estimated viscosities and thermal conductivities of gases at high temperatures. Tech. Rep. NASA TR R-132, National Aeronautics and Space Administration, Cleveland, Ohio
203. Institut für Arbeitsschutz der Deutschen Gesetzlichen Unfallversicherung. http://gestis.itrust.de (2018)
204. Smit B, Karaborni S, Siepmann JI (1995) J Chem Phys 102(5):2126. https://doi.org/10.1063/1.469563
205. Moore CE (1949) Atomic energy levels vol. 1. Tech. Rep. NBS Circular 467, US Government Printing Office, Washington
206. Ashpis DE, Laun MC, Griebeler EL (2017) AIAA J 55(7):2254. https://doi.org/10.2514/1.J055816
207. Sawada Y, Ogawa S, Kogoma M (1995) J Phys D Appl Phys 28(8):1661. https://doi.org/10.1088/0022-3727/28/8/015
208. Morent R, De Geyter N, Van Vlierberghe S, Dubruel P, Leys C, Gengembre L, Schacht E, Payen E (2009) Prog Org Coat 64(2–3):304. https://doi.org/10.1016/j.porgcoat.2008.07.030
209. Morent R, De Geyter N, Van Vlierberghe S, Dubruel P, Leys C, Schacht E (2009) Surf Coat Technol 203(10–11):1366. https://doi.org/10.1016/j.surfcoat.2008.11.008
210. Morent R, De Geyter N, Jacobs T, Van Vlierberghe S, Dubruel P, Leys C, Schacht E (2009) Plasma Process Polym 6(S1):S537. https://doi.org/10.1002/ppap.200931101
211. Bröcker L, Perlick GS, Klages C-P (2020) Plasma Process Polym e2000129. https://doi.org/10.1002/ppap.202000129
212. Loffhagen D, Becker MM, Czerny AK, Klages C-P (2020) Electrical characteristics of atmospheric-pressure DBD in argon with small admixtures of TMS—measured and calculated data. https://doi.org/10.34711/inptdat.250